2022-06

ADVANCING U.S. NAVY LOW-LIGHT UNDERWATER OPERATIONS

Green, Miguel A.

Monterey, CA; Naval Postgraduate School

http://hdl.handle.net/10945/70678

NAVAL POSTGRADUATE SCHOOL

MONTEREY, CALIFORNIA

THESIS

ADVANCING U.S. NAVY LOW-LIGHT UNDERWATER OPERATIONS

by

Miguel A. Green

June 2022

Thesis Advisor: James H. MacMahan
Co-Advisor: Tetyana Margolina

Approved for public release. Distribution is unlimited.

THIS PAGE INTENTIONALLY LEFT BLANK

REPORT DOCUMENTATION PAGE	Form Approved OMB No. 0704-0188

1. AGENCY USE ONLY *(Leave blank)*	2. REPORT DATE June 2022	3. REPORT TYPE AND DATES COVERED Master's thesis

4. TITLE AND SUBTITLE ADVANCING U.S. NAVY LOW-LIGHT UNDERWATER OPERATIONS	5. FUNDING NUMBERS N0001422WX01388
6. AUTHOR(S) Miguel A. Green	
7. PERFORMING ORGANIZATION NAME(S) AND ADDRESS(ES) Naval Postgraduate School Monterey, CA 93943-5000	8. PERFORMING ORGANIZATION REPORT NUMBER
9. SPONSORING / MONITORING AGENCY NAME(S) AND ADDRESS(ES) Office of Naval Research (Arlington, VA 22203-1995)	10. SPONSORING / MONITORING AGENCY REPORT NUMBER

11. SUPPLEMENTARY NOTES The views expressed in this thesis are those of the author and do not reflect the official policy or position of the Department of Defense or the U.S. Government.

12a. DISTRIBUTION / AVAILABILITY STATEMENT Approved for public release. Distribution is unlimited.	12b. DISTRIBUTION CODE A

13. ABSTRACT (maximum 200 words)

U.S. Navy research on extremely low-light (ELL) cameras in nighttime underwater operations is limited. This study aims to address this limitation in capability by quantifying the Teledyne Bowtech Limited Explorer Pro Low Light Monochrome Camera's performance in the field as a function of water depth at night in the coastal ocean. To reach this goal, proven techniques like modulation transfer function (MTF) and contrast transfer function (CTF) analyses were applied to modified target patterns for lower-quality images. The new target pattern was tested on land using commercial cameras against a commercial test pattern chart for high-resolution cameras. The ELL camera vertical casts, including measures of surface lux and the water column characteristics, were performed at California's Monterey Harbor and Bay in the presence of bioluminescence. The MTF results from the target pattern showed a steady MTF as the spatial frequency increased; the MTF decayed with increasing depth and decreasing lux. Furthermore, the MTFs showed that bioluminescence improves the MTF at depths ≥ 24.5 m versus the MTF with no bioluminescence. The target pattern was detected at a maximum depth of 37 m. However, predicted maximum depths using a linear regression model were > 37 m with and without bioluminescence. The new ideal target pattern for the ELL video camera provides a foundation for nighttime underwater operations and the future development of underwater night vision goggles for the U.S. Navy.

14. SUBJECT TERMS modulation transfer function, contrast transfer function, inherent optical properties, lux, low-light operations, low-light video camera, underwater video camera, night vision goggles, image quality test pattern, image quality test charts, MTF curve, bioluminescence, spatial frequency, zero crossing, chlorophyll, confidence interval, standard deviation, charge-coupled device, line pairs per millimeter, optical transfer function, Richard Bracker Research, extremely low light, visual acuity	15. NUMBER OF PAGES 61
	16. PRICE CODE

17. SECURITY CLASSIFICATION OF REPORT	18. SECURITY CLASSIFICATION OF THIS PAGE	19. SECURITY CLASSIFICATION OF ABSTRACT	20. LIMITATION OF ABSTRACT
Unclassified	Unclassified	Unclassified	UU

NSN 7540-01-280-5500

Standard Form 298 (Rev. 2-89)
Prescribed by ANSI Std. 239-18

THIS PAGE INTENTIONALLY LEFT BLANK

Approved for public release. Distribution is unlimited.

ADVANCING U.S. NAVY LOW-LIGHT UNDERWATER OPERATIONS

Miguel A. Green
Lieutenant Commander, United States Navy
BA, Thomas A Edison State College, 2011

Submitted in partial fulfillment of the
requirements for the degree of

MASTER OF SCIENCE IN METEOROLOGY AND PHYSICAL OCEANOGRAPHY

from the

NAVAL POSTGRADUATE SCHOOL
June 2022

Approved by: James H. MacMahan
Advisor

Tetyana Margolina
Co-Advisor

Peter C. Chu
Chair, Department of Oceanography

THIS PAGE INTENTIONALLY LEFT BLANK

ABSTRACT

U.S. Navy research on extremely low-light (ELL) cameras in nighttime underwater operations is limited. This study aims to address this limitation in capability by quantifying the Teledyne Bowtech Limited Explorer Pro Low Light Monochrome Camera's performance in the field as a function of water depth at night in the coastal ocean. To reach this goal, proven techniques like modulation transfer function (MTF) and contrast transfer function (CTF) analyses were applied to modified target patterns for lower-quality images. The new target pattern was tested on land using commercial cameras against a commercial test pattern chart for high-resolution cameras. The ELL camera vertical casts, including measures of surface lux and the water column characteristics, were performed at California's Monterey Harbor and Bay in the presence of bioluminescence. The MTF results from the target pattern showed a steady MTF as the spatial frequency increased; the MTF decayed with increasing depth and decreasing lux. Furthermore, the MTFs showed that bioluminescence improves the MTF at depths ≥ 24.5 m versus the MTF with no bioluminescence. The target pattern was detected at a maximum depth of 37 m. However, predicted maximum depths using a linear regression model were > 37 m with and without bioluminescence. The new ideal target pattern for the ELL video camera provides a foundation for nighttime underwater operations and the future development of underwater night vision goggles for the U.S. Navy.

THIS PAGE INTENTIONALLY LEFT BLANK

TABLE OF CONTENTS

THIS PAGE INTENTIONALLY LEFT BLANK

LIST OF FIGURES

THIS PAGE INTENTIONALLY LEFT BLANK

LIST OF TABLES

THIS PAGE INTENTIONALLY LEFT BLANK

LIST OF ACRONYMS AND ABBREVIATIONS

CCD	charge-coupled device
Chl_a	chlorophyll-a
CI	confidence interval
COTS	commercial-off-the-shelf
CTD	conductivity, temperature, and depth
CTF	contrast transfer function
DSLR	digital single-lens reflex
ELL	extremely low light
eSFR	edge spatial frequency response
HD	high definition
IOP	inherent optical properties
ISO	International Organization for Standardization
LG	Life's Good
Lp/mm	line pairs per millimeter
MTF	modulation transfer function
ND	neutral density
OTF	optical transfer function
RBR	Richard Bracker Research
STD	standard deviation

THIS PAGE INTENTIONALLY LEFT BLANK

ACKNOWLEDGMENTS

Thank you, God, for making all things possible. There were times when the journey to NPS seemed impossible, but through God, anything is possible!

I am grateful for my beautiful wife, Asaka, and our beautiful children, Kazuki and Maika. Thank you for your support and understanding throughout this journey and for letting me know what is truly important. You all have been the best part of my day: waking up, seeing your lovely faces, and coming home to you all every day.

My thanks go to my thesis advisors, Professor Jamie MacMahan and Dr. Tetyana Margolina. Jamie, thank you for your guidance, mentorship, and vision throughout our journey. I appreciate your allowing me to navigate this process my way, even though my methods are unorthodox. Tetyana, thank you for your time and dedication to this project. We spent numerous hours, days, nights, and weekends meeting on Zoom, working together on MATLAB, and in the field. Words cannot thank you enough!

To my friends, Alonzo Ingram, Shunika Johnson, Elias Nadaf, and Monica Killoran, thank you all and your families for the friendship, support, and love you have shown my family and me.

Lastly, I sincerely thank everyone who played an integral role in making my vision a reality.

THIS PAGE INTENTIONALLY LEFT BLANK

I. INTRODUCTION

The U.S. Navy is exploring the capability of extremely low-light (ELL) cameras for underwater nighttime operations to expand its competitive edge over adversaries. Research on ELL cameras is limited in the subaqueous environment relative to the subaerial optical developments at night with near-zero surface lux. For example, night-vision goggles are well-developed for military operations (Parush et al. 2011). The U.S. Navy does not have similar night vision underwater cameras or goggles for underwater nighttime operations (yet). There is a gap in nighttime underwater operations with optical technology that the U.S. Navy needs to address to maintain its competitive edge.

No such capability existed for ELL cameras for underwater nighttime operations until Moeller (2021) tested and validated the Teledyne Bowtech Limited Explorer Pro Low Light Monochrome Camera, referred to as the ELL video camera, which can operate underwater with near-zero surface lux (Moeller 2021). This ELL video camera detected objects underwater to a maximum depth of 25 m in the open ocean and 12 m in California's Monterey Harbor with low surface illumination. The ELL video camera exceeded expectations. The designed metrics to evaluate its performance were crude, including the visibility of Secchi disks at varying distances, human detection of a Snellen eye chart, and computer extraction of object edges. The metrics only qualitatively defined object detection that changed as a function of lux or water depth. Better "quantitative" techniques exist, but they are designed for high-resolution, high-quality cameras operating in static, high lux scenarios. New techniques are needed to quantify the ELL video camera visually due to its lower resolution, lower image quality associated with the video format and low-light operation, and movement throughout the water column.

Here, the goal is to quantify the ELL video camera's performance in the field as a function of water depth at night in the coastal ocean. To reach this goal, proven industry-standard techniques like modulation transfer function (MTF) and contrast transfer function (CTF) analyses were applied to modified target patterns for lower-quality images (Chapter II, Section A). The MTF represents the transfer function between the actual input image or target and the ELL camera's estimate of the target, which describes the camera's response

as a function of spatial frequency for underwater nighttime operations (Chapter II, Section A). Three target patterns are certified for estimating the MTF: the sine wave, slanted-edge, and square-wave patterns (Allen and Triantaphillidou 2010). This project evaluated the appropriate target pattern and adapted it for the ELL video camera (Moeller, 2021) (Chapter II, Section B). The new target pattern was tested on land using commercial cameras against a commercial test pattern chart for high-resolution cameras (Chapter II, Section C). ELL video camera vertical casts, including measures of surface lux and inherent optical properties of the water column (IOP) (Chapter II, Section D), were performed at Monterey Harbor (Chapter III, Section B) and the deeper depths of Monterey Bay (Chapter III, Section B). The MTF results from the target pattern show a steady MTF plot as the spatial frequency increases; the MTF decays with increasing depth and decreasing lux (Chapter III, Section B). The field tests were consistent with Moeller's (2021) results, including the bioluminescence bias (Chapter III, Section B). Comparing the bioluminescence and non-bioluminescence MTFs show that bioluminescence improves the MTF at depths $\geq$ 24.5 m versus the non-bioluminescence MTF (Chapter III, Section B). The new ideal target patterns for the ELL video camera provide a foundation for nighttime underwater operations and the future development of underwater night vision goggles for the U.S. Navy. The findings can be applied *a priori* for underwater mission outcomes.

II. METHODS

A. MTF AND IMAGE QUALITY TEST PATTERNS

Next, the equations and terminology applied to evaluate the ELL video camera's performance are described. All sceneries and targets within the ELL video camera's field of view are modified when the camera acquires the image. The degree of altering represents the camera's performance, which can be quantified. The acquired camera image, *o(x,y)*, is a two-dimensional convolution of the target, *m(x,y)*, with the transfer function of the camera, *h(x,y)*, written as

$$o(x, y) = m(x, y) * h(x, y), \tag{1}$$

where *x* and *y* are the image spatial coordinates, and *h(x,y)* is the camera's response to the lens quality, image processor, pixel resolution, and lighting. Applying the Fourier transform to the right-side of Eq. 1 results in the multiplication described by

$$O(u, v) = M(u, v) \times H(u, v), \tag{2}$$

resulting in an image spectra *O(u, v)*, where *M(u, v)* and *H(u, v)* are the Fourier transforms of the target and transfer function, respectively, and *u* and *v* represent spatial frequencies. The Fourier transform is the preferred approach over convolution owing to its programming simplicity (Fiske and Silverstein 2006). *H(u, v)* is referred to as the optical transfer function (OTF), which is a complex number defining the amplitude and phase response of the target in all orientations (Boreman 2001). The phase response is usually neglected since phase shifts are small (Lin and Chan 1997). The amplitude portion of the OTF is referred to as the MTF for defining the camera's ability to recognize contrasts and minute details of the target (Chen et al. 2008). The MTF is typically close to 1 for low spatial frequencies and decays with increasing spatial frequencies. The ratio of the complex amplitude, or modulus, of the Fourier transformed image to the amplitude of the Fourier transformed target represents the MTF, as suggested by Zhang et al. (Zhang et al. 2012) and defined as

$$MTF(u, v) = \frac{|O(u, v)|}{|M(u, v)|}. \tag{3}$$

Computing the MTF(u,v) requires an *a priori* accurate representation of $|M(u,v)|$, which is problematic for two reasons: the target location needs to be specific and printing a computer-generated target pattern reduces its quality (resolution, color). For example, if a defined target pattern is generated on a computer, the Fourier transform of this is represented by $|M(u,v)|$. However, the target pattern must be printed and placed in front of the camera for evaluation. Any misrepresentation of the printed target patterns will negatively bias the camera's performance. Furthermore, the target image is placed at differing distances with varying tilt angles, so georectification is required. Therefore, the process requires sophisticated image quality test pattern charts and corresponding processing. There are commercial-off-the-shelf (COTS) programs and test pattern charts, for example, through MathWorks and Imatest (Imatest 2022). However, the COTS charts are designed for high-resolution cameras operating with high lux settings. The charts and methods do not work for low-light, lower-resolution cameras (as described below). Thus, *a priori* estimates of $|M(u,v)|$ are not feasible for ELL cameras, so more rudimentary approaches to establishing the MTF are required.

Several COTS image quality test patterns have been developed to measure the MTF for cameras. These test patterns represent the target, $m(x,y)$, such as the sine wave, slanted-edge, and square-wave patterns (Allen and Triantaphillidou 2010) (Figure 1). A sine wave pattern is a continuous gradient that sinusoidally varies (Figure 1a-b), defined as Michelson contrast, and varies with differing spatial wavelengths (Nill 2001). The sine wave pattern avoids the harmonic distortion associated with the square-wave pattern (Boreman 2001). The contrast is based on the average of the lighter intensities greater than the grayscale midpoint relative to darker intensities less than the grayscale midpoint. The design and construction of sine wave target patterns are the most difficult to produce accurately for a test chart. Conversely, slanted-edge image quality test charts are the least computational (Zhang et al. 2012) and the least intuitive to the authors. The slanted-edge pattern is a single square or rectangle of a black and white region separated with a slight 4–6-degree slant relative to vertical or horizontal (Roland 2015) (Figure 1c). An estimated slant angle is obtained from the square or rectangle. The pixel intensities are transformed into an orthogonal line relative to the slant angle, representing the edge intensity profile. The

Fourier transform of the edge intensity profile represents the MTF (Fischer and Holm 1994). For the slanted edge, it is recommended that the number of pixels for the profile be around 50 to 100 long to maintain an adequate spatial frequency response (Masaoka et al. 2014). The square-wave pattern is the last suggested target and consists of a series of black and white bars that vary in spatial frequency and are reproduced accurately (Chen et al. 2008) (Figure 1d-e). The square-wave Fourier representation results in harmonics that bias the higher spatial frequencies. A zero-crossing approach is applied to evaluate each pair of black and white square waves in the spatial domain (Eq. 4) and is then described in the spatial frequency domain to avoid the generation of harmonics. Of the three test patterns, the square-wave pattern was deemed most appropriate for accurately generating a test chart in-house and its simplicity in its intuitive understanding of the results. The square-wave pattern also allows for a range of spatial frequencies that can match the capabilities of the proposed ELL video camera with its lower resolution and image graininess that occurs in nighttime settings in underwater applications.

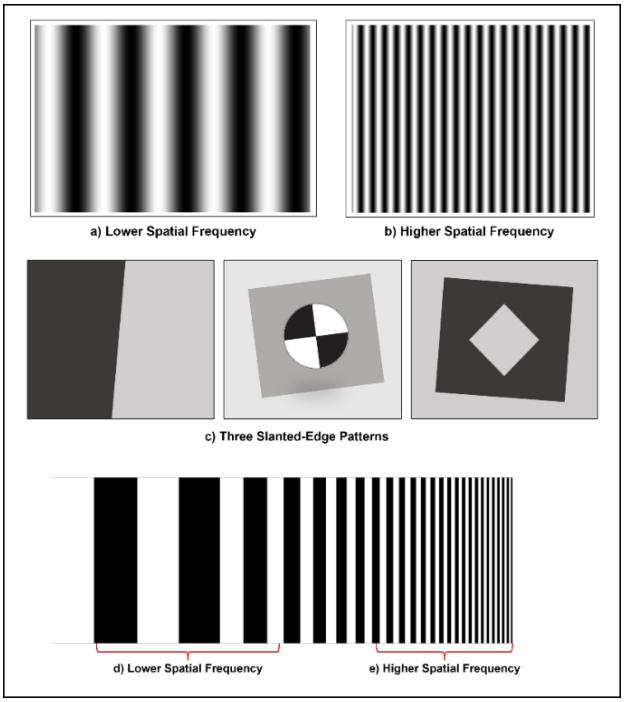

(a) Lower Spatial Frequency Sine Wave. (b) Higher Spatial Frequency Sine Wave. (c) Three Slanted Edge Patterns. (d) Lower Spatial Frequency Square Wave. (e) Higher Spatial Frequency Square Wave.

Figure 1. Image quality test patterns.

Utilizing the square wave pattern, an MTF can be estimated by evaluating varying spaced pairs of black and white lines and their relative contrast. The contrast is defined as

$$Contrast = \frac{I_{\max} - I_{\min}}{I_{\max} + I_{\min}}, \tag{4}$$

where I_{max} and I_{min} are the maximum (white lines) and minimum (black lines) light intensities for consecutive line pairs in the image. The line pairs are well-resolved if the contrast is close to 1 and are not well-resolved for contrast percentages close to 0. The spatial frequency is the inverse of the wavelength between the line pairs. As the spatial frequency increases, the lines blur as the contrast decreases. As the spatial frequency continues to increase, eventually, optical systems cannot distinguish between the black and white line pairs, which signifies the camera's limit to resolve fine-scale details. Ultimately, the image's black and white lines will appear as one uniform gray line. The contrast between the black and white lines is typically normalized by the first line pair relating the percentage of contrast as a function of spatial frequency, measured in line pairs per millimeter (lp/mm) (Leung and Donnelly 2017). The CTF describes the rate of contrast reduction of the target during the imaging process (Wang et al. 2014). The CTF represents the modulation of the line pairs and is described by

$$CTF(f) = \frac{C_{output}(f)}{C_{target}(f)}. \tag{5}$$

In Eq. 5, C_{output} and C_{target} are the contrasts of the acquired camera image and the original target, respectively. The contrast of the target is assumed to be 1, which means the contrast of the acquired image is precisely the value of the CTF (Wang et al. 2014). The CTF is based on a square-wave target pattern, like the patterns used in this study, while the MTF is based on a sine-wave target pattern. However, the CTF is related to the MTF by

$$MTF(f) \cong \frac{\pi}{4} \times CTF(f), \tag{6}$$

where $\frac{\pi}{4}$ is the amplitude of the fundamental frequency of the square wave (Coltman 1954).

B. IMAGE QUALITY TESTS CHARTS (COMMERCIAL AND IN-HOUSE)

Imatest's Edge Spatial Frequency Response (eSFR) International Organization for Standardization (ISO) slanted-edge test charts were selected to quantify the ELL video camera (Figure 2a). As indicated by Imatest, these slanted edge charts automatically calculate several image-quality factors such as sharpness, lateral chromatic aberration, tonal response, color response, and noise measurements following the ISO 12233:2014 standard (Imatest 2022). Also, Imatest's slanted-edge charts use space efficiently and provide repeatable results. Imatest's photographic eSFR and extended eSFR inkjet ISO test charts were utilized herein. The edges of the 15 slanted gray boxes measure the spatial frequency response and lateral chromatic aberration or color fringing, which denotes image sharpness. The chart's four Secchi disks or registration points detect orientation and automatically detect the regions of interest for measurements. The 20-patch optoelectronic conversion function grayscale pattern surrounding the center of the chart is used to measure the camera's tonal response, gamma, white balance, and noise. Lastly, the Tetris-like color patches measure the camera's color accuracy, and the hyperbolic wedges determine limiting resolution and moiré fringing.

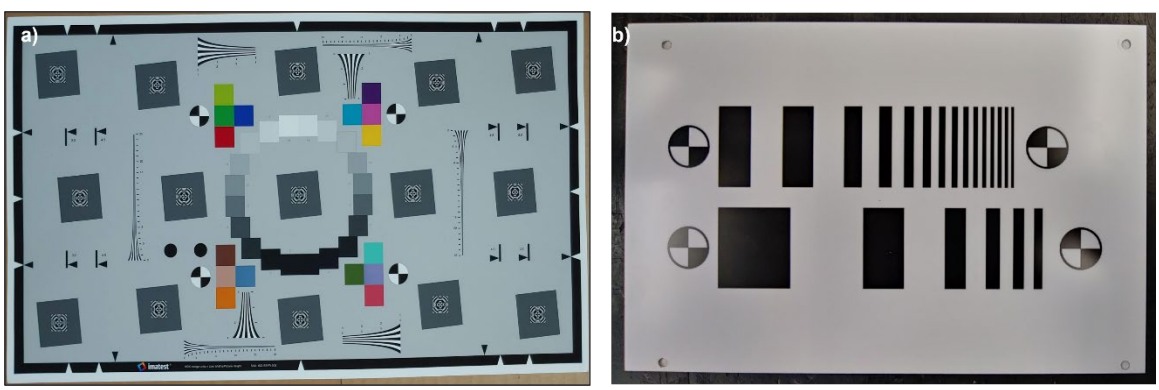

(a) Imatest's Edge Spatial Frequency Response International Organization for Standardization (ISO) slanted-edge test chart. (b) High and low-frequency square wave patterns.

Figure 2. Selected image quality test charts.

High and low-frequency square wave patterns were developed in-house to match better and evaluate the visual acuity of the ELL video camera (Figure 2b). The size and spatial frequency of the square-wave patterns were adjusted to maximize the camera's visual acuity underwater and resolution for ELL conditions. The high-frequency square wave pattern at the top of the image comprises 15 separate line pairs of black and white rectangular bars, and the low-frequency square wave pattern has six line pairs of black and white rectangular bars. The two pairs of registration points, centered outside the patterns, are for estimating pixel pitch to convert spatial frequencies from line pairs/pixel to lp/mm. The camera's CTF is measured by analyzing captured images of the alternating black and white bars at finer spatial scales (Leung and Donnelly 2017). The printed test pattern is on waterproof material to conduct field experiments in an undersea environment. The first iteration of this pattern was 3-D printed on a Delrin sheet. However, after several field tests, the elevated surface of the black bars cast shadows onto the white bars, which contaminated the CTF calculation for that spatial frequency. Thus, a flat surface chart is best for calculating the CTF, so the high- and low-frequency square-wave patterns were printed onto a 203.2 mm x 304.8 mm aluminum sheet for evaluating the camera's performance in low-light field conditions.

Zero crossings of the square-wave pattern on the target are required to delineate regions of white and black for computing contrast in the CTF (Figure 3). In addition, zero crossings estimate wavelength for defining spatial frequencies. Typically, zero crossings are computed for each image. Here, the zero crossings are calculated with the best image and applied to the corresponding images, as decreasing lux zero-crossings become inaccurate. Zero crossings are defined horizontally where the intensity passes through zero (defined as the grayscale mean), representing the edges of the black and white bars. Consecutive zero-crossings define regions, and successive down crossings represent the wavelength. Owing to the graininess of the images in ELL, the median intensity includes measures over the length of the vertical bar to increase confidence and more accurately describe the signal relative to noise.

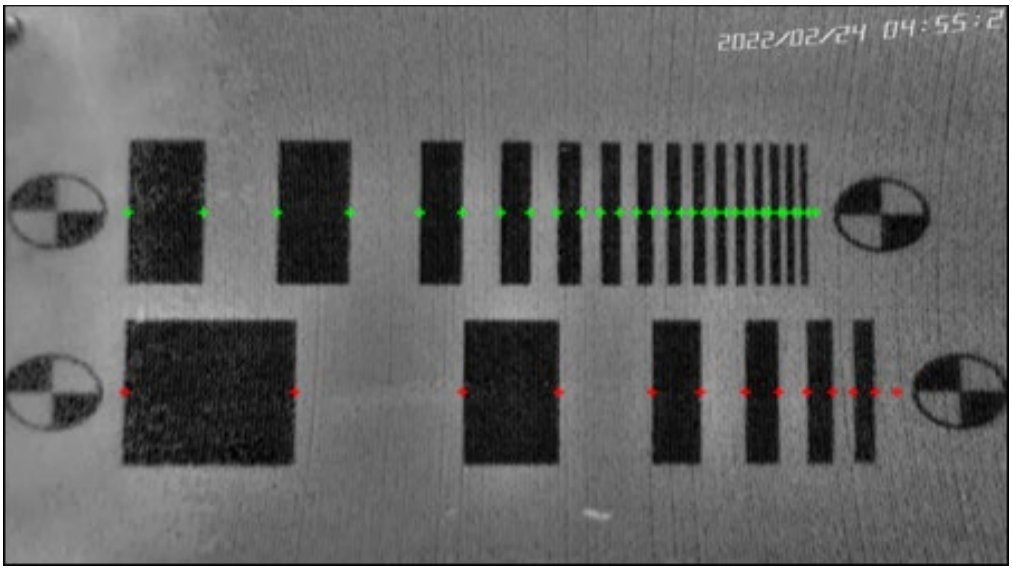

Figure 3. Computed zero crossings.

Spatial frequencies can be calculated either as line pairs/pixel or as a reciprocal of the corresponding wavelength. Two reference points were applied to convert the spatial frequencies into line pairs/mm, one pair per square-wave pattern. Multiplying any line pairs/mm by two equates the total lines per millimeter. Taking the reciprocal of the total lines per millimeter determines the size, in millimeters, of individual distinguishable objects. For example, a spatial frequency of 1 lp/mm is equivalent to 2 lines/mm (one black line, one white line). Taking the reciprocal of 2 lines/mm equals 0.5 mm, which means at a spatial frequency of 1 lp/mm, individual objects 0.5 mm or larger are distinguishable. In conclusion, a pixel pitch or linear horizontal size of an image pixel was calculated as a ratio of the total pixel distance between corresponding reference points and a known distance in millimeters.

C. CAMERA SETUPS AND LENS CALIBRATION

Numerous low-light sensitivity experiments were conducted by capturing images of the Imatest eSFR and square-wave charts at various luxes and comparing the MTF curves. These experiments validated the in-house test chart for the following field research in a low-light undersea environment. Images of the test pattern charts were taken with two cameras that operated without a flashlight. One was a Life's Good (LG) G8 ThinQ

smartphone with dual rear cameras of standard angle and super wide-angle at 12 and 16 megapixels of resolution. The second was a Canon EOS 60D digital single-lens reflex (DSLR), autofocus, and autoexposure camera with an 18-megapixel complementary metal-oxide-semiconductor sensor.

The Teledyne Bowtech Limited Explorer Pro Low Light Monochrome Camera is an enhanced security video camera housed in an underwater vessel designed for depths up to 2,000 m (Figure 4a). The ELL video camera utilizes a 12.7 mm charge-coupled device image sensor coupled to a wide-angle, high-speed aspherical auto-iris lens allowing for a low light sensitivity of 2×10^{-5} lux (Teledyne Bowtech Ltd 2020). Due to the deployment depths, a self-contained secondary underwater pressure vessel houses a Talitor Hidden Video Recorder-D1 logger and a 12 Vdc 50 Wh Li-ion rechargeable battery for powering the camera (Figure 4b). The Li-ion battery provides more than 10 hours of power. The video logger was set to five frames per second and recorded AVI-formatted video to a Kingston Canvas Select 32 GB MicroSDHC Class 10 MicroSD Memory Card UHS-I. There are three available options for recording video, by a magnetic switch, by remote control, and the third option is via scheduled recording. An external monitor is available to validate camera operations for pre-and post-deployment recording and video playback. Lastly, the video camera is powered by turning an external switch.

The proposed MTF analysis requires a torsional rigid underwater frame to precisely capture the target's contrast and prevent target movement (Figure 4a). The MTF approach described herein defines the image regions of dark and light contrast for an ideal image obtained near the surface. The pixel regions are continuously applied throughout the images as a function of depth. If the chart shifts relative to the camera, pixel intensities are incorrectly described, skewing the MTF. Image shifting occurred when the camera equipment was mounted to a single metal I-beam. The I-beam twisted when cast in the ocean, notably when it reached the seabed. The I-beam was later reinforced with two 12.7-mm-thick, 304.8 mm x 609.6 mm Delrin sheets. Four 12 mm stainless steel threaded rods connected the two Delrin sheets, like bedposts, to provide a sturdier frame. The camera equipment was placed in various locations on the frame for ballasting and maintaining a rigid structure.

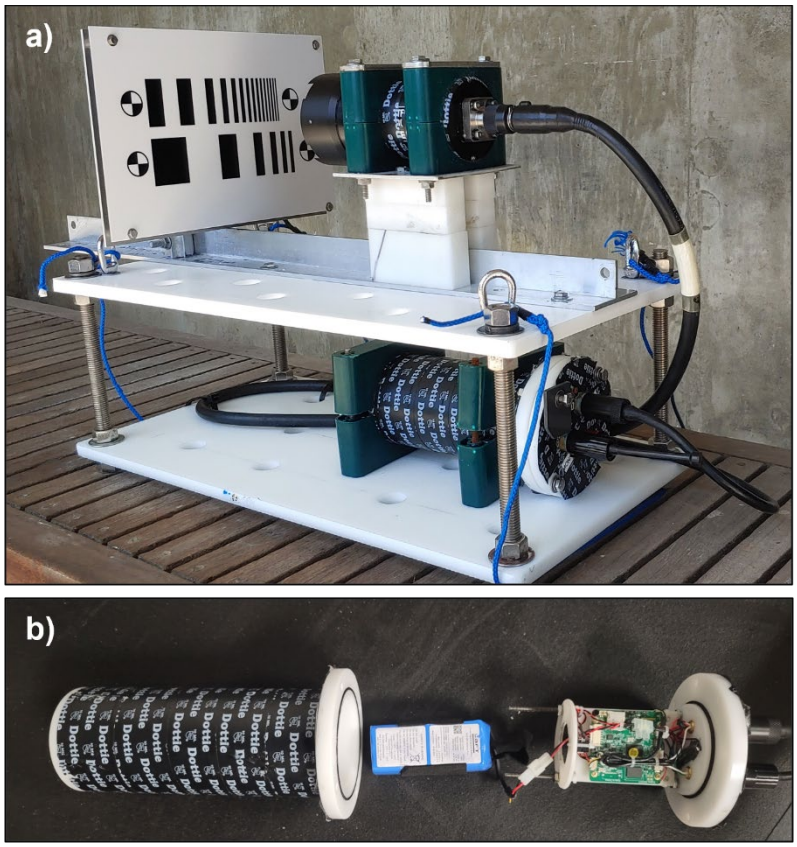

(a) The Teledyne Bowtech Limited Explorer Pro Low Light Monochrome Camera is connected to the underwater frame setup for field experiments.

(b). Housing setup for Video Recorder-D1 logger and Li-ion rechargeable battery for powering the camera. Source: (Moeller 2021).

Figure 4. ELL video camera, frame, and housing.

The ELL video camera's lens distortion (Figure 5a) was calibrated with a target composed of 7 x 10 square checkerboard patterns (Figure 5b). A checkerboard pattern was chosen because it is quickly produced with high accuracy (Liu et al. 2018). The calibration process determines the video camera's intrinsic and extrinsic parameters related to 2-D image pixels relative to 3-D world points (Figure 5d-e). After calibration, the lens distortion from the image can be removed (Miller and Al Badi 2020) (Figure 5c). The approach required multiple images of the checkerboard from differing views and distances (Figure 5e). The captured images, the pattern selection, the checkerboard size, and the distortion type were inputted into a commercially available camera calibrator (MATLAB Camera Calibrator; (MathWorks 2022) to estimate lens distortion. The calibration only needed to

be performed once because the target and camera were stationary. The images were collected at different distances from 145 mm to 200 mm (Figure 5e). The standard model calibration algorithm extracted the points detected on the checkerboard (green o) and the checkerboard origin (0, 0), (yellow □) (Figure 5b). The distance in pixels between the detected points and the corresponding reprojected points (red +) are the reprojection errors. Standard calibration accuracy is achieved when the reprojected points are centered inside the detection points or at a mean distance of less than one pixel from the detection points (MathWorks 2022).

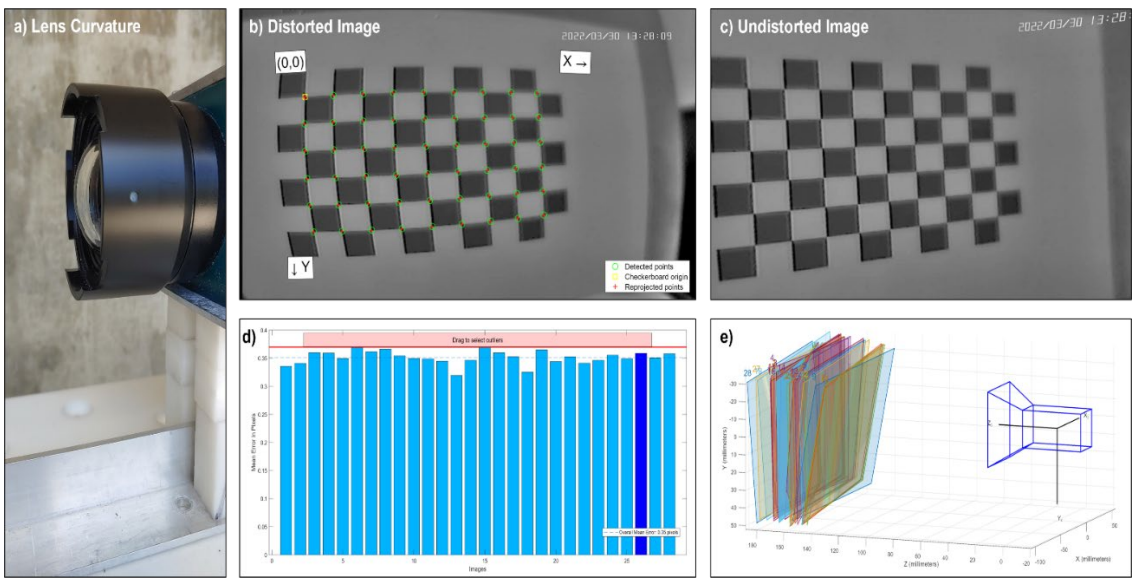

(a) Close view of ELL video camera's aspherical lens. (b) Detected points on the 7 x 10 checkerboard calibration pattern. (c) Undistorted image after applying camera calibration. (d) Reprojection errors bar graph. (e) 3-D extrinsic parameters plot for camera-centric view.

Figure 5. Evaluation of camera calibration results.

D. ENVIRONMENTAL MEASUREMENTS

Generally, the scattering properties of the water column and seawater constituents determine the result of image transmission (Hou 2013). Inherent optical properties (IOP) are the scattering and absorption properties of the water column and are measured frequently because of their importance in ocean optics. IOPs can describe the optical properties of the light transmission from the surface through the water column (Mobley

2022). One of the main issues concerning the ELL video camera's image transmission is that it directly depends on natural light. Still, the amount of available nighttime light is not always predictable from a tactical advantage standpoint. Accordingly, to measure the IOPs, a Richard Bracker Research (RBR) Maestro^3 multi-channel logger was profiled for conductivity, temperature, and depth (CTD), colored dissolved organic matter (CDOM), pressure, turbidity, salinity, and chlorophyll-a (Chl_a) throughout the vertical water column (Figure 6a). The RBR Maestro^3, referred to as CTD, was mounted in a protective metal cage and lowered separately by hand at the exact locations and depths of the video camera casts. The separate casts were to avoid added light sources from the optical sensor that could bias the ELL camera's image transmission. The CTD was time-synchronized with the ELL video camera and provided instantaneous water column profiles at a sampling rate of 2 Hz.

(a) RBR Maestro^3 multi-channel logger. (b) RBRsolo D sensor. (c) Extech EA30 wide range light meter.

Figure 6. Sensors used for environmental measurements.

An RBRsolo D sensor was attached to the ELL video camera's frame, adjacent to the camera, to investigate ocean pressure and depth as the frame transited the water column (Figure 6b). The RBRsolo D sensor and video camera were time synced before casting and used to create plots of the ELL camera versus time as a function of depth. This data helped synchronize the ELL camera video with graphs to determine the descending and ascending characteristics of the ELL camera's frame.

Environmental surface illumination was measured with the Extech EA30 wide range light meter (Figure 6c). The light meter operates at luxes greater than 1×10^{-2}, whereas the video camera works at luxes greater than 2×10^{-5}. Consequently, the video camera exceeds the light sensitivity of the light meter.

E. EXPERIMENTAL SUMMARY OF CHART VALIDATION AND FIELD TESTS

Both higher resolution cameras, the LG G8 ThinQ smartphone and Canon EOS 60D DSLR, were employed to enable detection of the registration points of the captured images of the Imatest chart, which were not obtainable when taken by the ELL video camera due to its lower resolution. The first test chart MTF comparison experiment was performed using the in-house square wave chart against the Imatest chart. The charts were placed 66 cm from the camera with controlled luxes of 30.1, 27.7, 0.9, and 0.02. The registration points of the Imatest chart could be detected at all luxes except 0.02 lux. A second test chart comparison was needed to ensure there were no discrepancies in the procedures. The second chart MTF comparison experiment was conducted using the same setup, although with a separation distance of 40 cm. Thor Labs Reflective Neutral Density (ND) Filter Kit controlled the lighting and further reduced luxes below 0.02 lux. Eight chart images were taken using filters ND01A (0.1 lux), ND02A (0.06 lux), ND03A (0.04 lux), ND04A (0.02 lux), ND10A (0.01 lux), ND20A (0.001 lux), ND30A (0.0001 lux), and ND40A (0.00001 lux).

III. RESULTS

The experimental procedures for image performance evaluation of the ELL video camera were performed through a series of land image quality tests using COTS charts and cameras and ocean image quality tests using the ELL video camera and an in-house developed chart. Under controlled lighting, the land tests were performed with high-resolution cameras against COTS test pattern charts. The brightness of the illumination varied with each experiment to represent a real-world nighttime ocean environment to determine the ideal test pattern to integrate into an underwater frame setup for field tests. Subsequently, in-house test charts were developed for two reasons: they were compatible with commercial software and exploitable in low- illumination environments of 0.02 lux and lower, representing minimum nighttime illuminations for military operations. Lastly, vertical ocean casts were performed from harbor docks and nearshore to evaluate the visual acuity of the ELL video camera as a function of ocean depth.

A. TEST CHART VALIDATION

The second test chart MTF land comparison experiment, using the smartphone and DSLR higher resolution cameras, confirmed that at lux measurements of 0.02 and lower, the images of the Imatest chart were too dark to detect the details required for computer analysis, so an MTF could not be calculated (Figure 7a), but the information on the chart could be visually seen in the images. Conversely, the registration points and spatial frequencies were detected at 0.02 lux and lower for the in-house square wave pattern chart (Figure 7b).

For both higher resolution cameras, over-sharpening proved to be a factor in their MTF calculations for the Imatest chart. The MTF for the smartphone was higher than the theoretical maximum of 1 and reached a peak at 0.1 spatial frequency (Figure 8a). When an MTF is higher than 1, it is due to forced over-sharpening of the image, typical of smartphones (Dugonik et al. 2020). It was hypothesized that the DSLR camera would not over-sharpen the images. Over-sharpening was relatively reduced when comparing the smartphone with the DSLR camera's MTF for the same Imatest chart (Figure 8b). Over-

sharpening was not an issue at lower spatial frequencies for the smartphone and DSLR camera when the MTF was calculated for the square wave chart. Consequently, the DSLR camera was employed to capture all subsequent land images because it was less susceptible to over-sharpening.

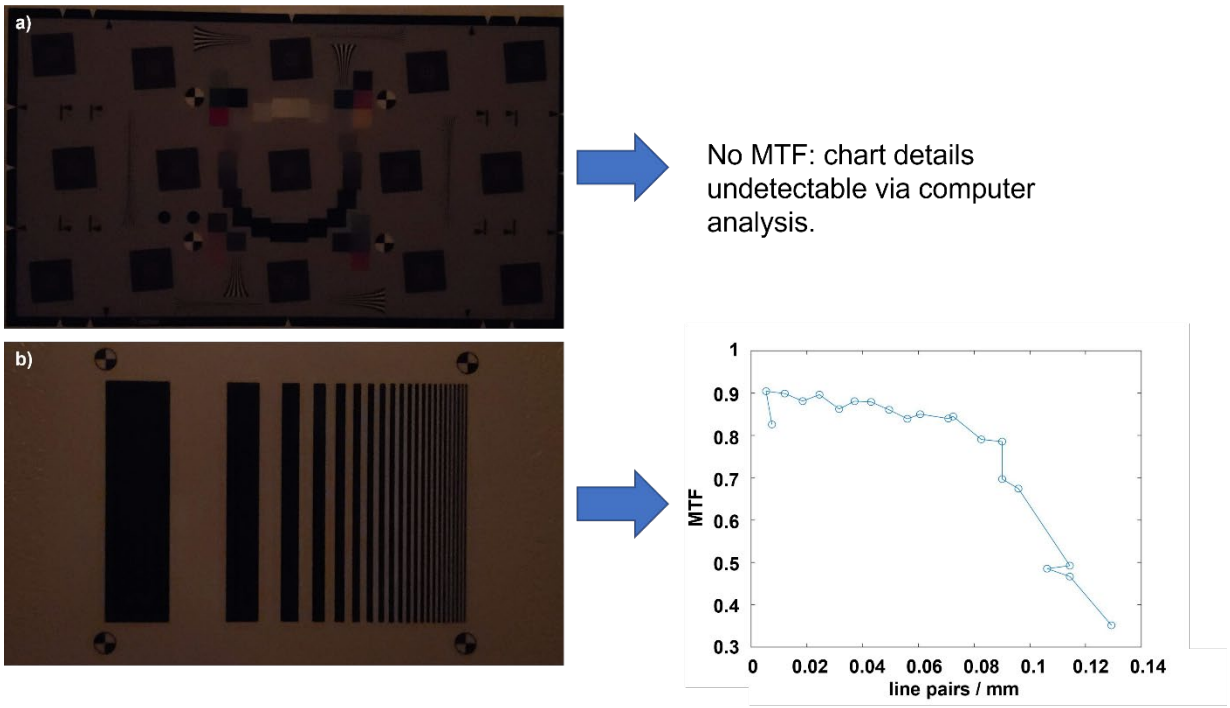

(a) LG G8 ThinQ smartphone image of Imatest Chart. (b) LG G8 ThinQ smartphone of a square wave pattern.

Figure 7. Second test charts MTF comparison at 0.02 lux.

The results from the test charts' MTF comparison experiments further validated why the in-house chart was chosen for field tests instead of the Imatest chart. The Imatest chart is only suitable for high lux environments with illumination greater than 0.02 lux, not representing a nighttime tactical ocean environment. In contrast to the in-house chart, the Imatest chart was affected by compatibility problems with MATLAB software. Imatest's software is built on MATLAB software but does not integrate directly with MATLAB software. Additionally, Imatest does not recommend laminating their charts for ocean field experiments since Imatest has no control over how the lamination process/material will

affect the chart's sharpness, contrast, and color/tone. Imatest's chrome-on-glass charts are the only waterproof charts that Imatest offers, but the charts require a backlight and are too small for testing at a distance. Therefore, conducting field tests in an undersea environment using the Imatest chart was not feasible.

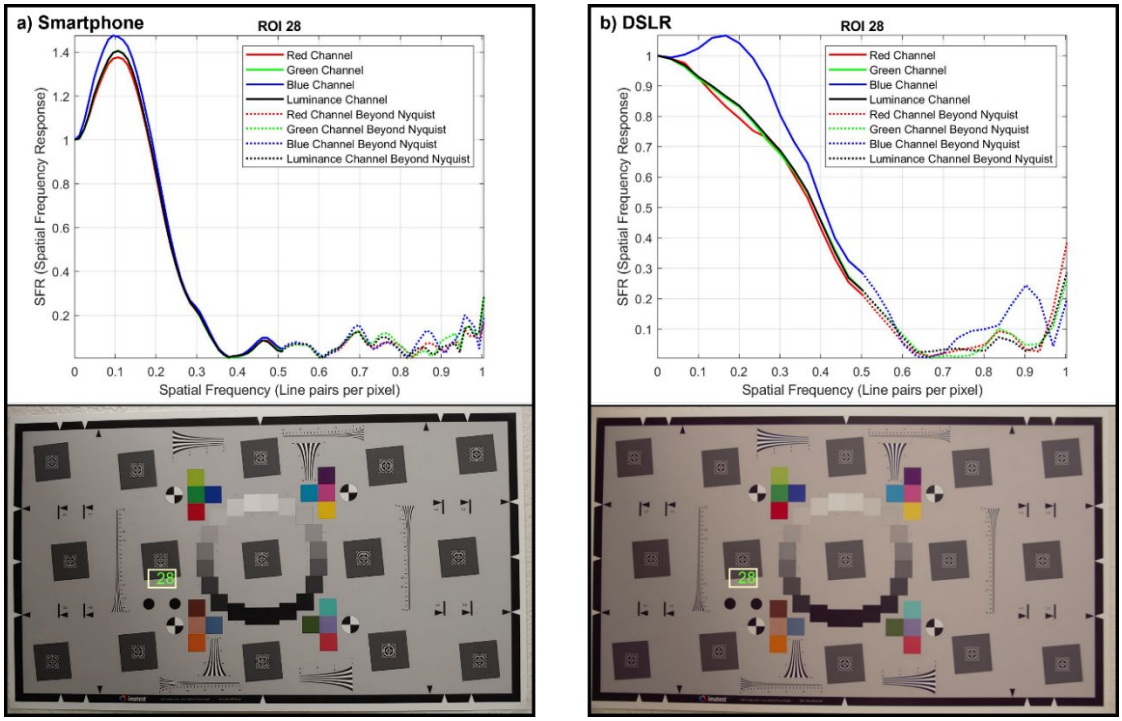

(a) The MTF is above one for the LG G8 ThinQ smartphone RGB channels. (b) The MTF curve is above one for the Canon EOS 60D DSLR only for the blue channel.

Figure 8. Smartphone and DSLR MTF comparison.

B. FIELD TESTS: MONTEREY HARBOR AND MONTEREY BAY

Vertical casts of the ELL video camera were performed at three locations along the Breakwater Cove Marina docks (Figure 9a) on three separate night deployments and a day deployment. The deployment depths ranged from 8–12 m. Before each deployment, a surface lux was taken and ranged from 0.01 to 0.15 for the night deployments and 31.28 to 47 kilolux for the day deployment. The vertical casts consisted of slowly (7 cm/s) lowering the video camera frame with a horizontal-look orientation from the dock until the frame touched the bottom of the seafloor, resting for about 60 s. Letting the frame rest on the

bottom enabled the ELL camera's auto-iris lens to adjust. Next, the frame was raised expeditiously (7.5-8.5 cm/s) until recovered. Separate CTD casts were performed at similar speeds before or after each video camera deployment. Only one of the three different night harbor experiments incorporated the sturdier frame with the Delrin sheets. In contrast, two of the three separate night experiments and the day experiment occurred using the less sturdy frame.

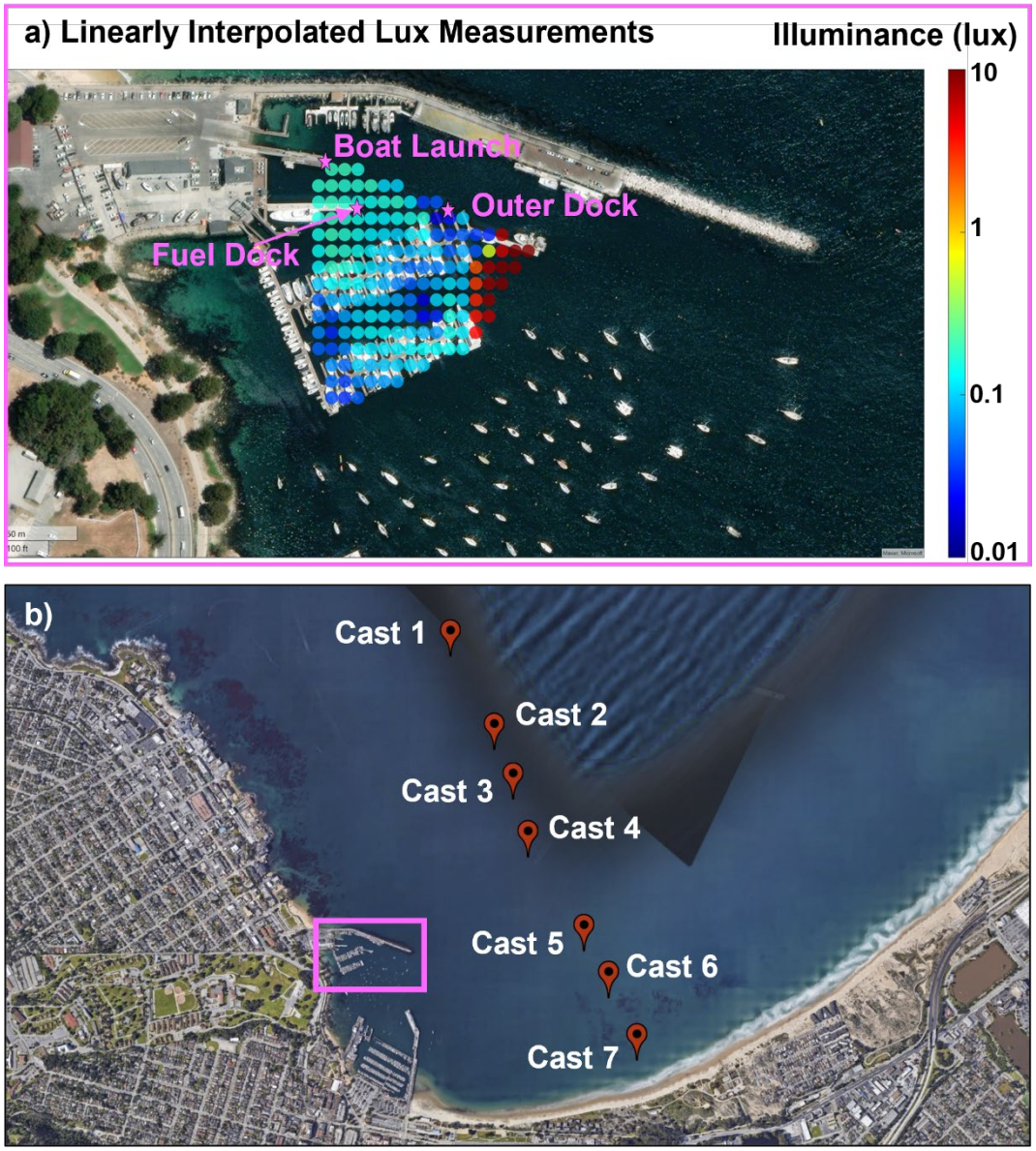

(a) Breakwater Cove Marina. (b) Open ocean cast location in Monterey Bay.

Figure 9. Monterey Harbor and Monterey Bay field test locations.

The boat launch and outer dock deployments were selected because they represented the highest and lowest lux and the shallowest and deepest depths at Breakwater Cove Marina (Figure 10). The near-surface images captured the lowest percentage of contrast of the square wave patterns, resulting in the lowest MTF values near the surface (Figure 10a-b). The boat launch near-surface MTF was the lowest across all casts. The higher lux from the harbor lights contributed to the contrast loss in the captured images, reducing the MTF. Inversely, the MTF for the bottom depths exhibited the lowest target contrast loss, resulting in higher MTF values than near the surface (Figure 10c-d). Although the bottom depths displayed higher MTF values, all plots maintained MTFs between 0.4-0.6 across all spatial frequencies.

The MTF plots for the boat launch and outer dock casts averaged over the bottom images and downcast and upcast images per 2 dbar bins are shown in figures 11 and 12, with standard deviation (STD) shown as error bars. The bottom MTF plot was the highest at the boat launch compared to the downcast and upcast. With a surface lux of 0.05, there was enough illumination for the ELL camera to detect fine details on the chart during the downcast and upcast and at a bottom depth of 6.6 m. The difference in MTFs was because the camera was stationary on the bottom, which enabled the ELL camera time to adjust. The ELL video camera continuously adapted to the changing environment during the upcast and downcast. Conversely, for the outer dock, the downcast displayed the highest overall MTF values as a function of depth compared to the upcast and bottom. The difference in the MTFs is because the ELL video camera was slowly lowered, enabling the camera to adjust. In contrast, the ELL video camera adjustments differed on the upcast, likely related to how the auto-adjustment was internally implemented. With a surface lux less than 0.01, there was enough illumination for the ELL video camera to detect fine details on the chart. However, the lower illumination reduced the contrast percentage of the image at the outer dock compared to the boat launch. The lower contrasted images and deeper depth at the outer dock contributed to the lower MTFs as a function of depth. Lastly, near the surface, both images displayed a consistent spread among the three plots caused by the loss in contrast of the target from the constant movement of the frame entering the water and expeditious recovery.

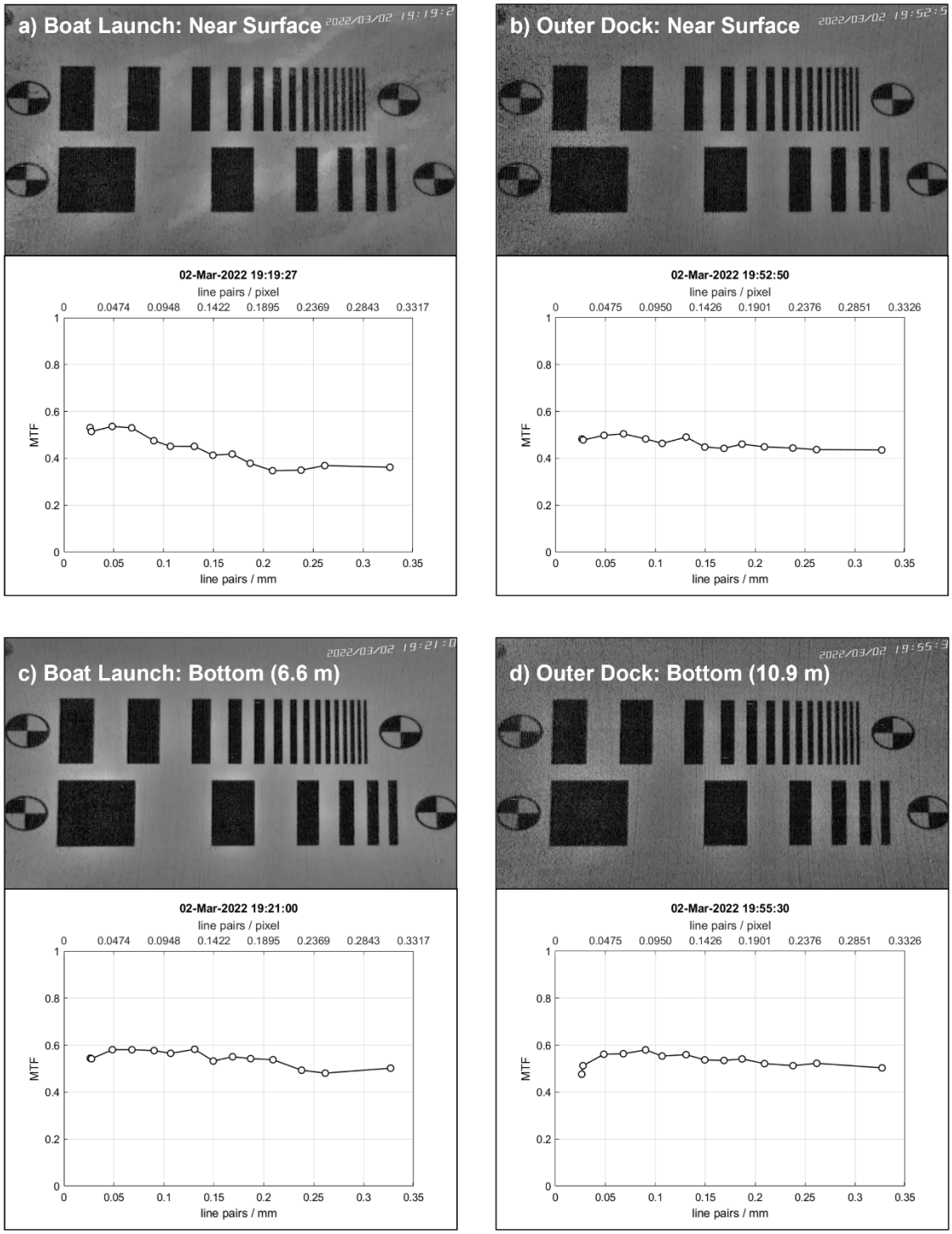

(a) Boat launch near-surface image and MTF plot. (b) Outer dock near-surface image and MTF plot (c) Boat launch bottom image and MTF plot at 6.6 m.(d) Outer dock bottom image and MTF plot at 10.9 m.

Figure 10. Monterey Harbor near-surface and bottom images and MTF plots.

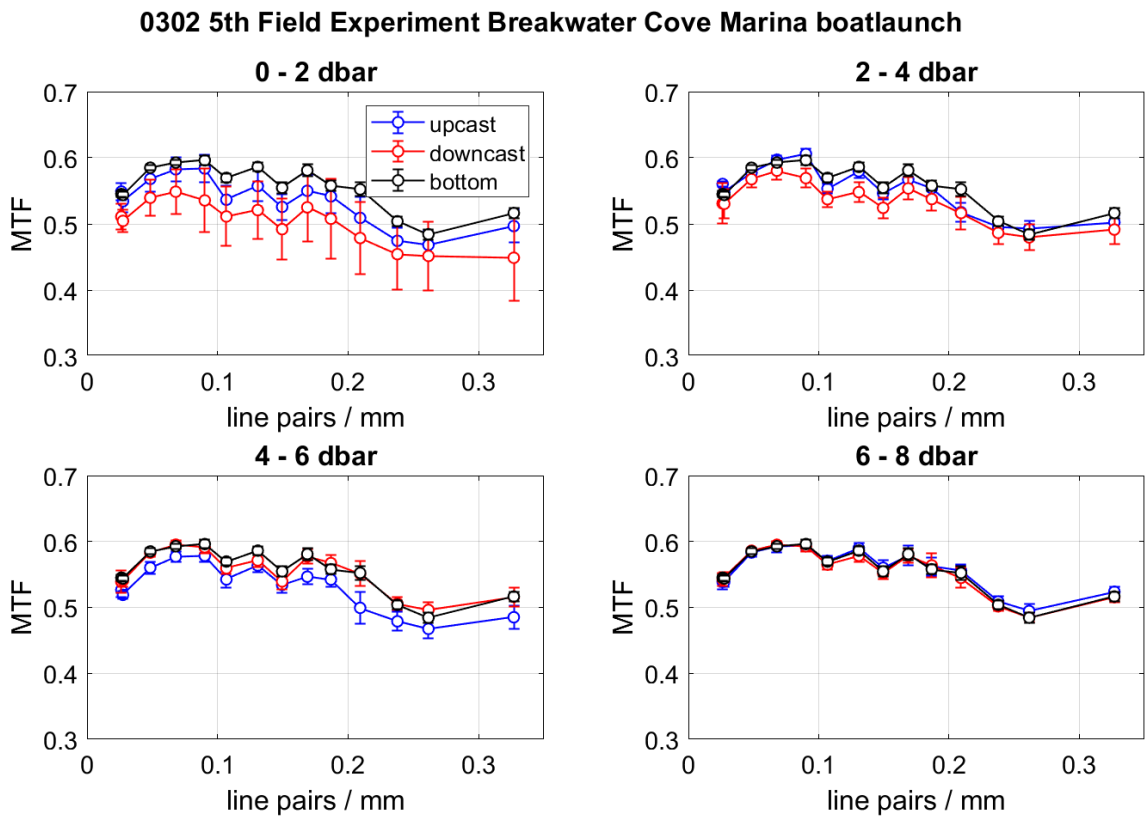

The error bars show the STD.

Figure 11. Mean MTF for the boat launch cast per 2-dbar bins.

The Monterey Harbor night experiments demonstrated the ELL video camera's capability to transfer the chart's information to image information at largely ≥ 45% for the near-surface MTF and ≥ 50% for the bottom MTF at all three locations. The near-surface and bottom plotted confidence intervals (CI) and STD for the MTF plots at the three locations are shown in Figure 13. The STD and CI are calculated for the 2-dbar bin range. The CI was calculated at the 95% confidence level, described as

$$CI = \overline{MTF} \pm 1.96SE = \overline{MTF} \pm 1.96\frac{s}{\sqrt{n*}}, \tag{7}$$

where $\overline{MTF}$ is the 2-dbar bin average, SE is the standard error, and s is the STD (Dowdy et al. 2004). With n equal to the number of independent MTF estimates within each bin. A

5-second running average was applied before the averaging by pressure. Thus, the CI calculation divided the total number of individual estimates by 25 (5 images per second, 5-second window).

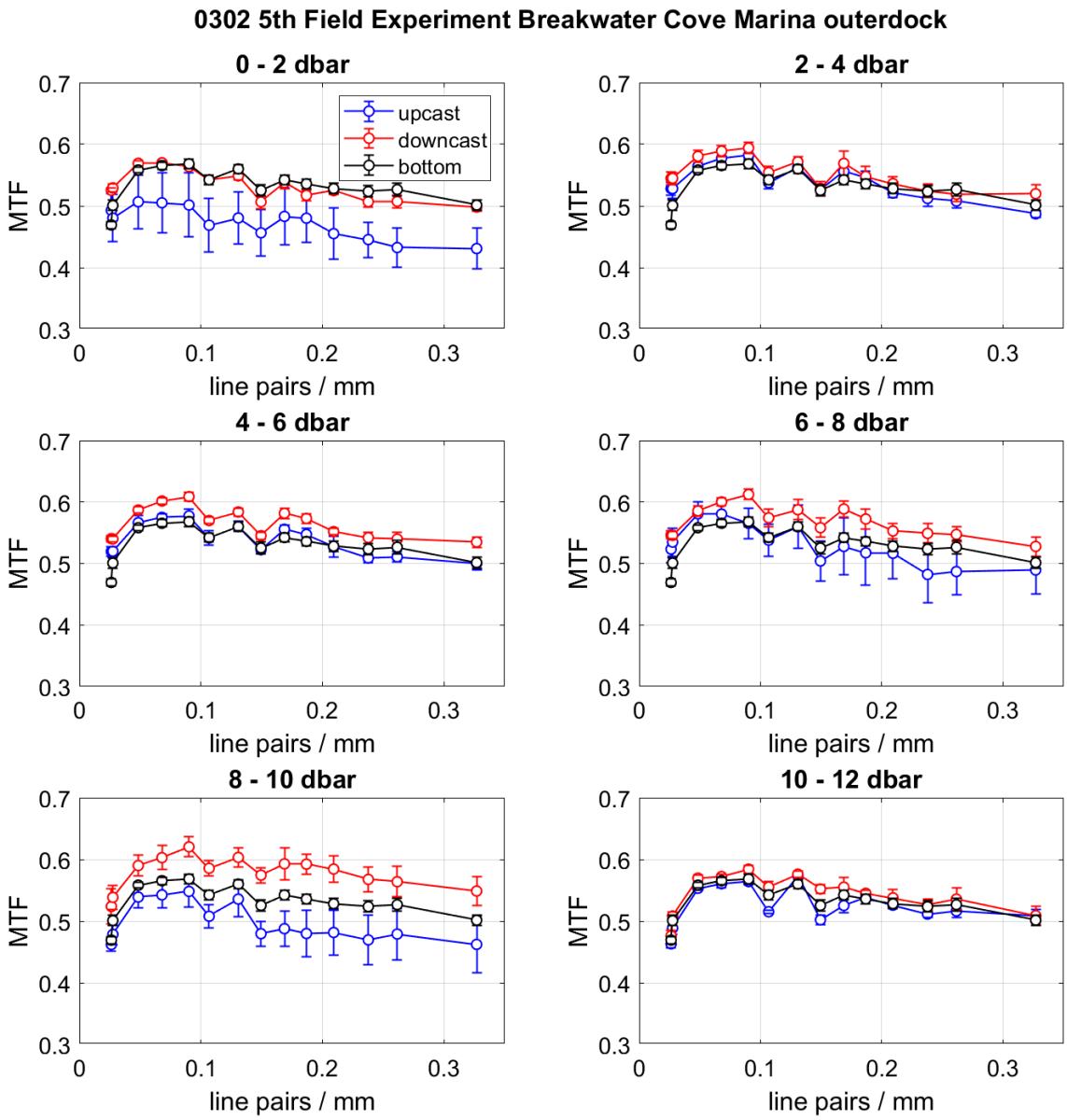

The error bars show the STD.

Figure 12. Mean MTF for the outer dock cast per 2-dbar bins.

All three harbor locations showed a small spread at lower spatial frequencies, and the spread widened at higher spatial frequencies for the near-surface and bottom estimates (Figure 13). The fuel dock displayed the highest MTF near the surface with increasing spatial frequency. The higher MTF resulted from less contrast loss near the surface because of artificial illumination from the harbor lights. A 0.02 surface lux was measured at the fuel dock, which was lower than the boat launch (0.05 lux) but higher than the outer dock (< 0.01 lux). In comparison, the boat launch and fuel dock displayed identical bottom MTFs until the spatial frequency increased above 0.2 lp/mm (Figure 13c-d). The outer dock had the lowest recorded surface lux and the deepest cast depth, resulting in the highest loss of target contrast and lowest MTF but still above 50% as spatial frequency increased above 0.3 lp/mm.

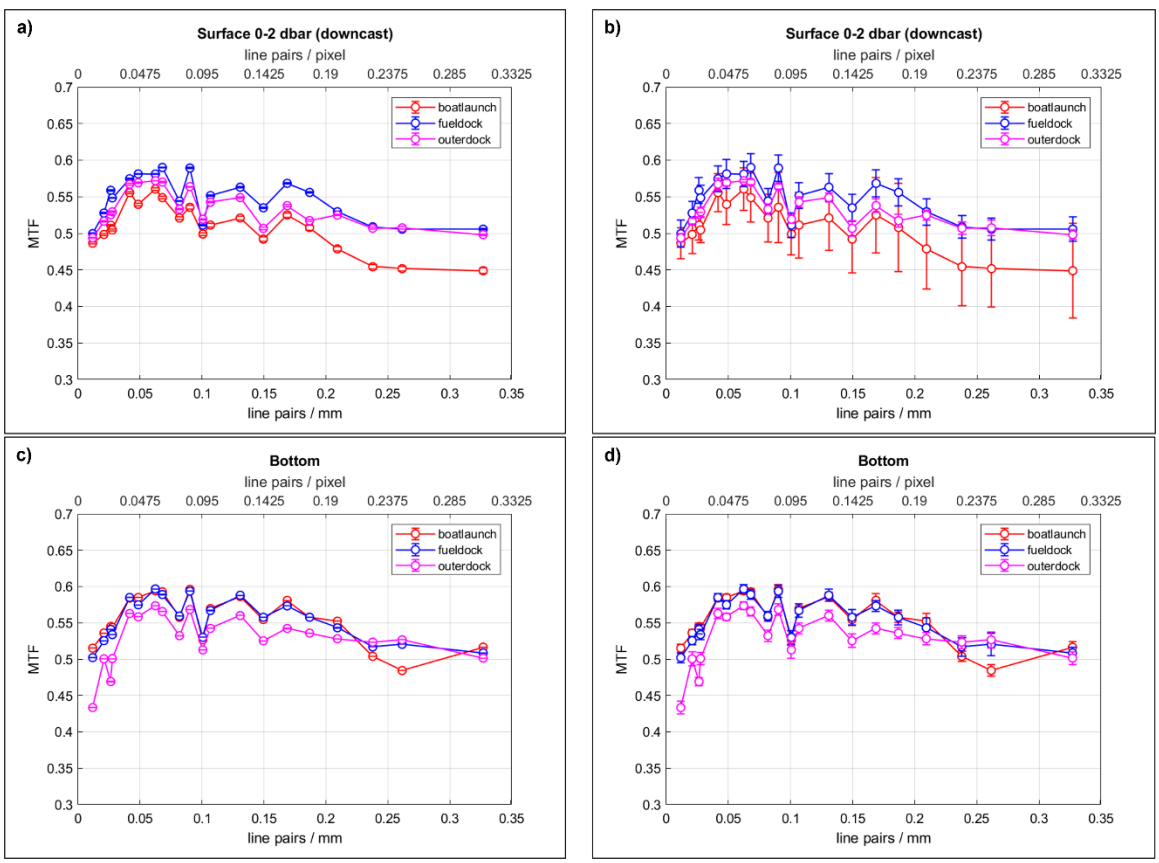

(a) Near-surface MTF CIs for the three cast locations. (b) Near-surface STDs for the three cast locations. (c) Bottom MTF CIs for the three cast locations. (d) Bottom MTF STDs for the three cast locations.

Figure 13. Monterey Bay near-surface and bottom CI and STD plots.

The downcast, bottom, and upcast MTFs were consistent for all three experiment locations in the Monterey Harbor (Figure 14). The bottom MTF for the boat launch was higher as the depth was not deep or dark enough for significant contrast loss of the target and resting the ELL video camera on the bottom for more than 60 s provided ample time for the camera's adjustment (Figure 14a). Out of the three MTFs, the fuel dock had the lowest spread among the downcast, upcast, and bottom plots, while the outer dock had the widest spread among its MTF plots (Figure 14b-c). The broader spread among the MTFs contributes to the previously mentioned environmental conditions. Furthermore, the outer dock MTF for the upcast was the lowest because the expeditious recovery of the ELL video camera did not allow the camera time to adjust to the changing IOPs throughout the water column.

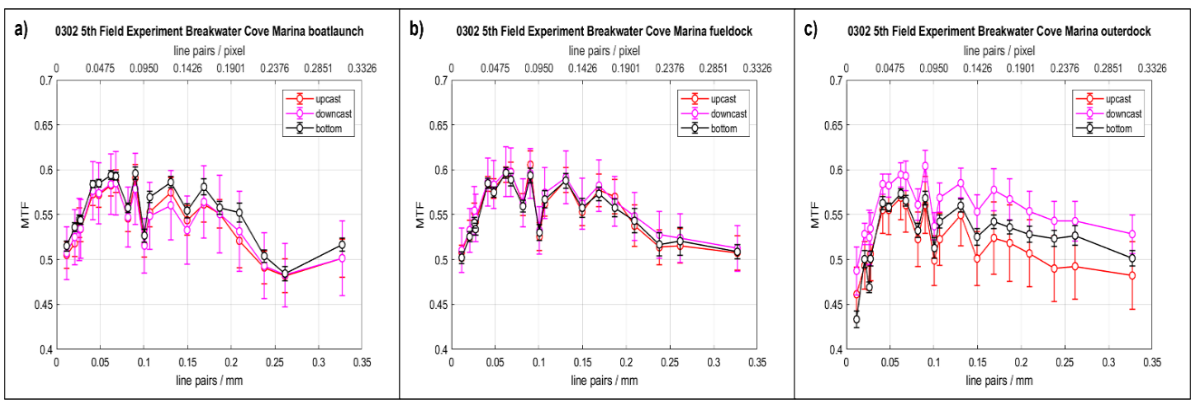

(a) Boat Launch upcast, downcast, and bottom MTF plots. (b) Fuel Dock upcast, downcast, and bottom MTF plots. (c) Outer Dock upcast, downcast, and bottom MTF plots.

The error bars show the STD.

Figure 14. Mean MTF plots for the Monterey Harbor casts per 2-dbar bins at all three locations.

The analyzed images of the Monterey Harbor experiments provided valuable information that revealed further research was needed to test the limits of the video camera. The maximum depth at the Monterey Harbor docks was 12 m. Moeller's (Moeller 2021) open-ocean vertical casts experiments showed that the ELL video camera could detect objects on a chart at depths up to 25 m. Thus, there was no doubt that the ELL video camera could capture the contrast at various spatial frequencies on the square-wave chart at depths

up to 25 meters and farther. To test this hypothesis, measurements needed to be taken at deeper depths and under natural light conditions away from the harbor.

The Monterey Bay deployment occurred on a cloudless morning before sunrise on February 24, 2022, with 42% of the moon's visible disk illuminated and no visual evidence of bioluminescence. This deployment was the inaugural deployment of the revamped frame consisting of the 12.7-mm-thick Delrin sheets. Seven separate vertical casts were performed (Figure 9b) starting at 44 m, 33.8 m, 30 m, 24.6 m, 19.5 m, 14.5 m, and 10 m, following the same procedures as the harbor casts; additionally, a peanut float was attached to a smaller rope connected to the frame and the lowering-rope to prevent the lowering-rope from covering any portion of the chart. Besides the depth, the first cast in 44 m of seawater was different from the other casts for three reasons. First, the video camera's frame was slowly lowered to 37 m, held for 60 s, and did not touch the bottom before being recovered. Second, the video camera's frame was lowered to 37 m to test the maximum visual acuity depth of the camera, which was hypothesized to be 35 m. Third, it was assumed that the bioluminescence intensity would be low and not interfere with the transfer of fine details from the chart to the camera if the camera's frame was not stationary. All subsequent casts were slowly lowered to the bottom, resting for 60 s, and then expeditiously recovered using similar procedures as the Monterey Harbor casts. These casts were lowered to the bottom to allow the video camera's frame to remain stationary to mitigate bioluminescence contamination by not agitating the phytoplankton. Four separate CTD casts were performed in conjunction with every other video camera cast, starting at a depth of 44 m. The measured luxes were not credible due to the sensor's wetness, particularly the 34.3 lux. The moon's illumination was at 42%, equivalent to an estimate of less than 0.23 lux. According to Nowinszky and Puskás (Nowinszky and Puskás 2012), the minimum and maximum illumination values for a new moon and full moon vary between 0.001 lux and 0.23 lux at the surface. The lowest lux recorded during the Monterey Bay experiment, 0.05 lux, will be used as a reference.

Moon illumination provided the surface illumination for the Monterey Bay experiment. The ELL video camera's near-surface images captured the highest percentage of contrast of the square wave patterns, resulting in the highest MTFs near the surface

across all casts (Figure 15a-c); conversely, the MTFs for the bottoms and deepest depth exhibited the highest target contrast loss, resulting in the shallow MTFs (Figure 15d-f). However, none of the MTFs showed a substantial dip as the spatial frequency increased. There was a 20% spread in the MTFs for near-surface and the bottom at the deeper depths, while shallower depths ($\leq$ 14.5 m) displayed less spread. The MTFs across all spatial frequencies showed an inversely proportional relationship to ocean depth. As the ocean bottom depth decreased with subsequent casts, the MTFs increased in percentage.

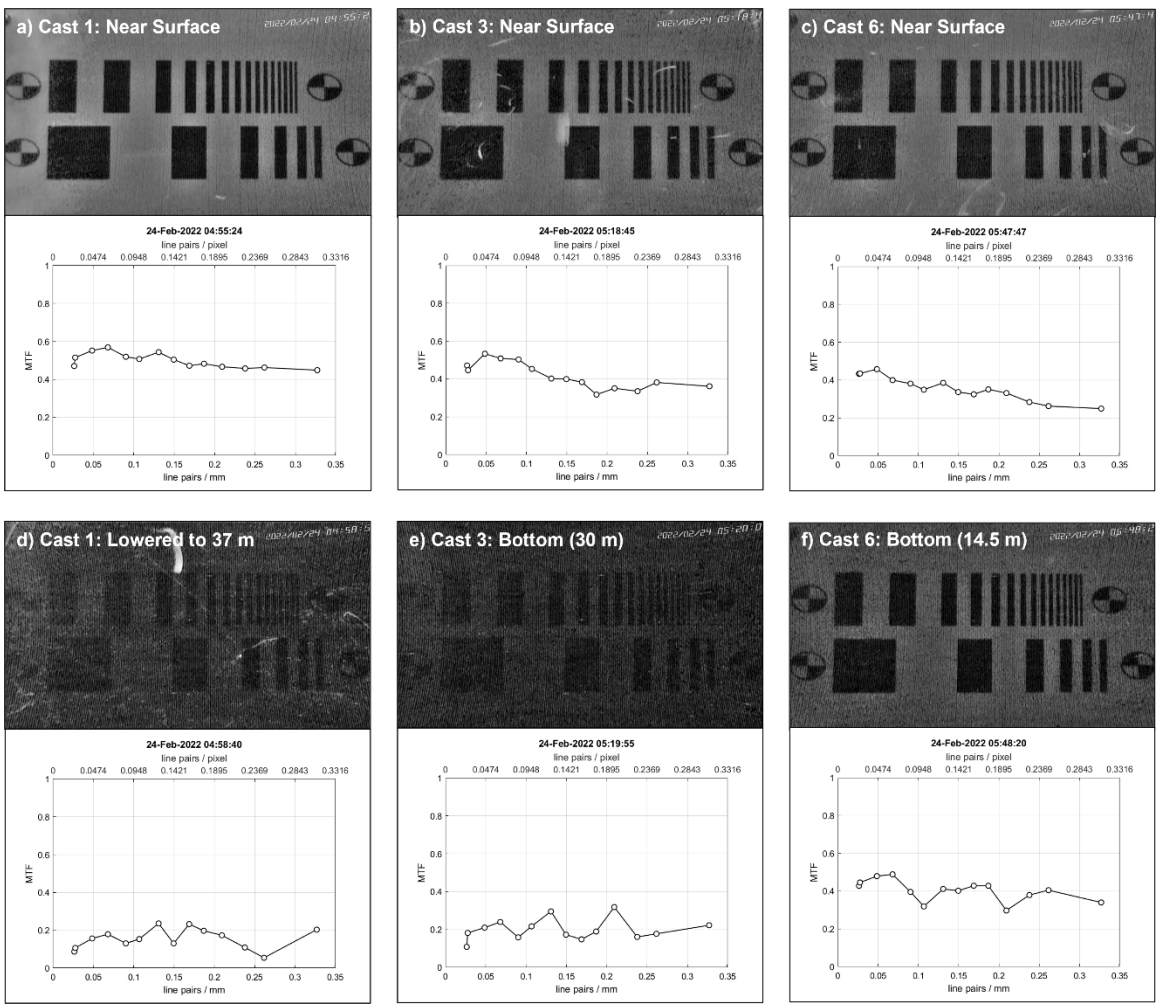

(a) Cast 1 near-surface image and MTF plot. (b) Cast 3 near-surface image and MTF plot. (c) Cast 6 near-surface image and MTF plot. (d) Cast 1 lowered to 37 m image and MTF plot. (e) Cast 3 bottom image and MTF plot at 30 m. (f) Cast 6 bottom image and MTF plot at 14.5 m.

Figure 15. Monterey Bay near-surface and bottom images and MTF plots.

Four CTD casts were performed in the Monterey Bay in conjunction with every other ELL video camera deployment and paralleled with changes in water depth of 10 m. Profiles 1–3 displayed consistent levels of Chl_a throughout the water column that ranged as high as 5 mg/L (Figure 16).

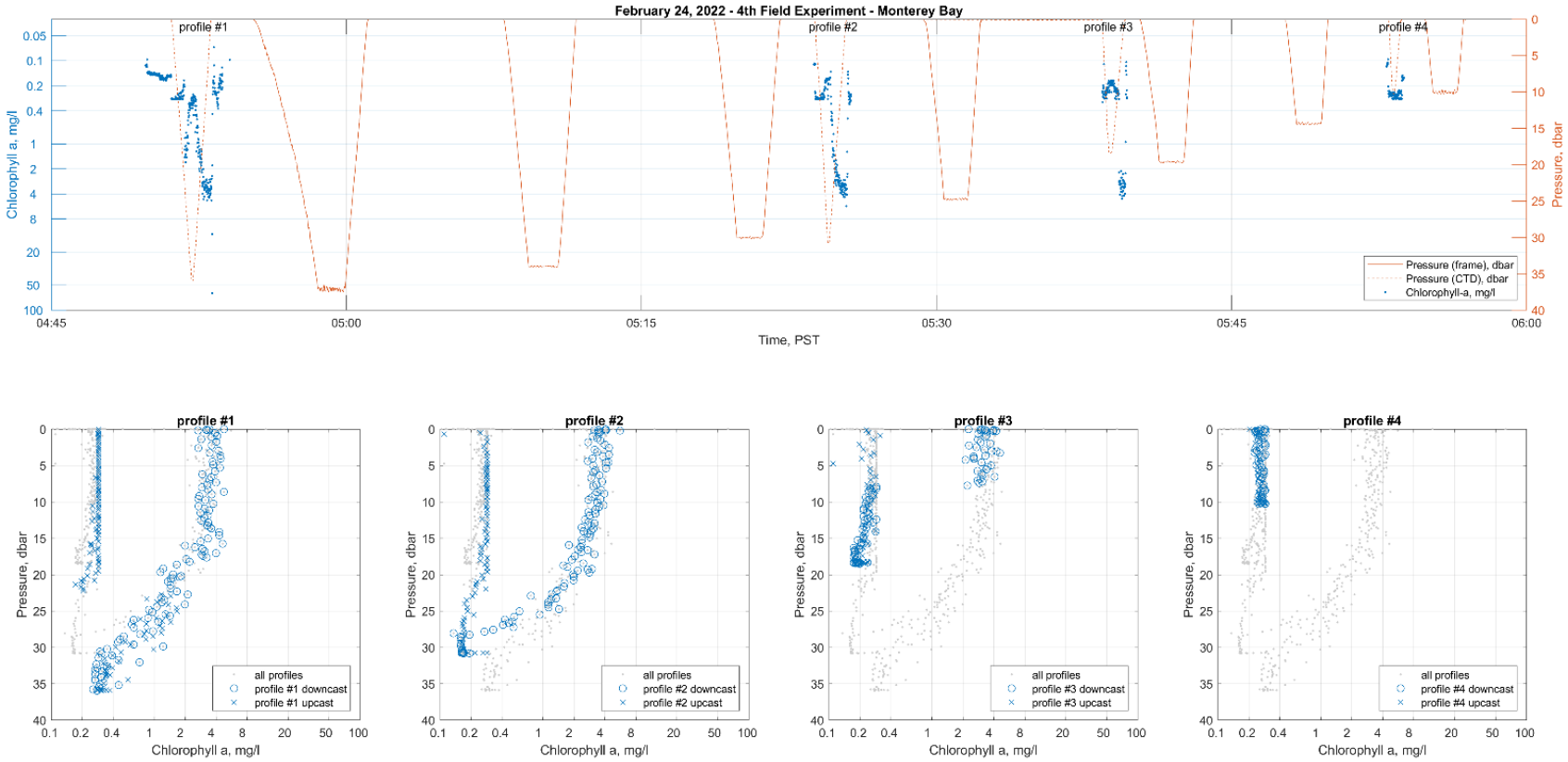

Figure 16. Monterey Bay chlorophyll-a plots for four profiles.

The analysis of the results was consistent with the higher bioluminescence with depth, as shown in the captured image (Figure 15d), compared to the lower Chl_a levels in the Monterey Harbor, which showed much lower bioluminescence contamination of the images. The influence of bioluminescence on image contrast and subsequent calculation of MTFs were plotted (Figure 17). The downcast and bottom MTFs were plotted for six separate cast and depths. The downcast and bottom MTFs were compared to reference MTFs since these exhibited the least amount of bioluminescence contamination across all casts. The remaining cast MTFs were calculated when the ELL video camera was not stationary but at a depth equivalent to the bottom depth. This approach was utilized to differentiate the non-bioluminescence influenced (bottom) from the bioluminescence affected images (all casts excluding the bottom) until the maximum downcast depth of 37 m was reached. The bottom MTFs outperformed the bioluminescence-influenced MTFs until 24.5 m. The bioluminescence-influenced MTFs exceeded the bottom MTFs as the illumination and target contrast decreased significantly with increased ocean depth.

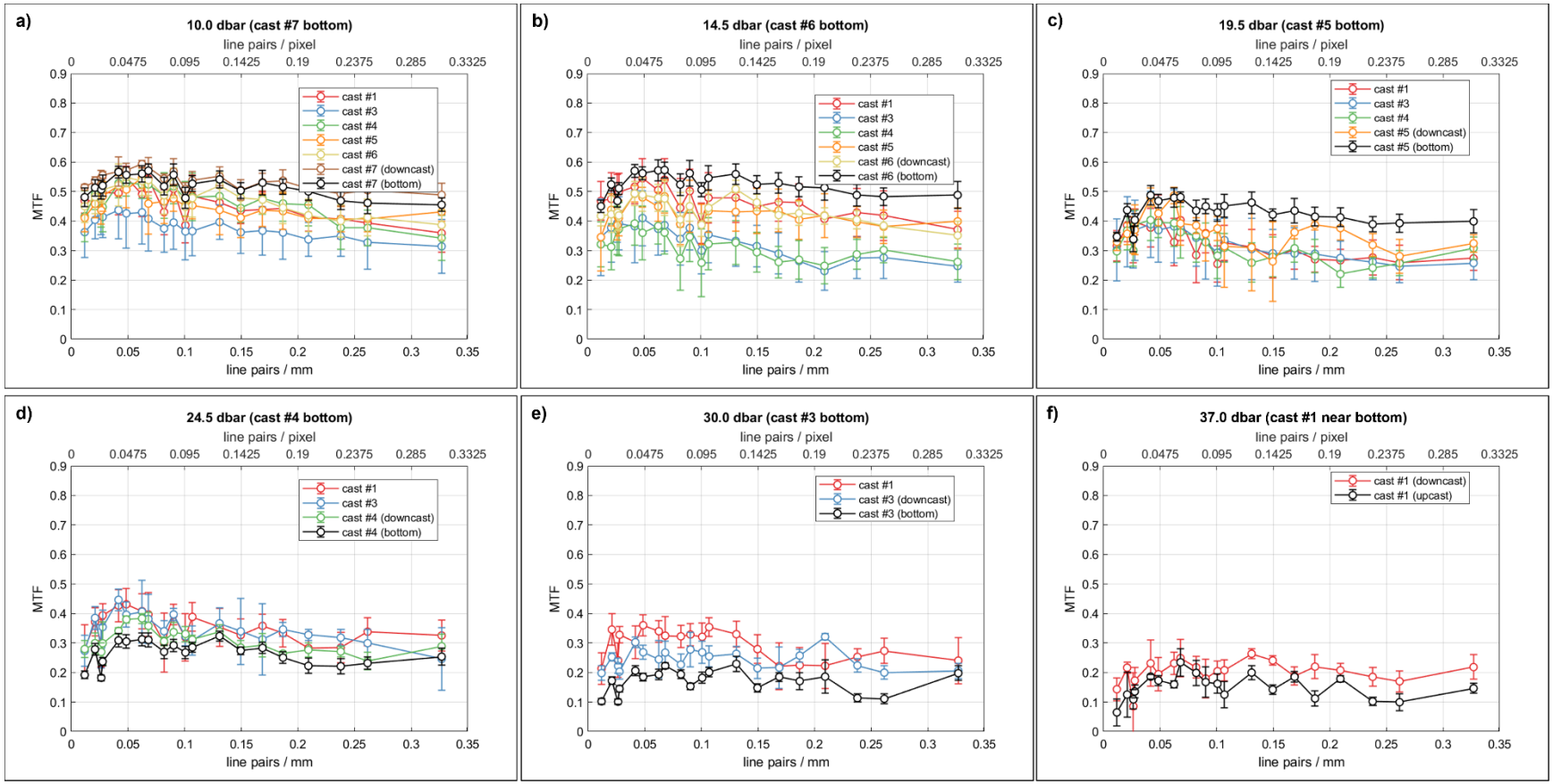

(a) Cast #7 downcast and bottom (non-bioluminescence) vs. moving casts #1, #3-6 (bioluminescence) at 10 dbar. (b) Cast #6 downcast and bottom (non-bioluminescence) vs. moving casts #1, #3-5 (bioluminescence) at 14.5 dbar. (c) Cast #5 downcast and bottom (non-bioluminescence) vs. moving casts #1, #3-4 (bioluminescence) at 19.5 dbar. (d) Cast #4 downcast and bottom (non-bioluminescence) vs. moving casts #1, #3 (bioluminescence) at 24.5 dbar. (e) Cast #3 downcast and bottom (non-bioluminescence) vs. moving cast #1 (bioluminescence) at 30 dbar. (f) Cast #1 downcast (non-bioluminescence) and upcast (bioluminescence) at 37 dbar.

Figure 17. Non-bioluminescence vs. Bioluminescence influenced MTF. Error bars show STDs.

IV. DISCUSSION

A. COMPARISON WITH NVGS

The U.S. military has a long history of exploiting night vision goggles (NVG) to enhance its image quality at night in low-light land environments. The MTF can express the image quality of NVGs; however, there is no prototype to compare with the results. The purpose of evaluating the image quality performance of optical systems is to establish a metric that provides the user with an expectation of the system's visual performance (Task and Pinkus 2007). MTF results for underwater ELL cameras are also incomparable to other ELL cameras due to limited research. Although there is not an ideal metric to compare the MTF results for NVGs, the results can provide valuable insight compared with the MTF results of the ELL video camera, even though both capabilities operate in separate environments.

The distinction between visual acuity measurement techniques for NVGs and the ELL video camera is substantial. First, the ELL camera is a post-processed video camera as it is challenging to send divers down for testing. The NVG on land tends not to have video logging and therefore is evaluated by humans. NVG visual acuity measurements require subjective or objective observations typically made by a person looking through NVGs at the test pattern target (Task 2001). One of the frequently used test patterns to qualitatively evaluate the performance of U.S. military optical systems is the 1951 USAF tri-bar chart. However, according to Task and Pinkus (2007), studies have indicated discrepancies > 59% in observer response when using the tri-bar pattern. Conversely, for this project, the MTF was computed on the ELL images of the test pattern images, removing human bias.

B. AUTO-IRIS LENS ADJUSTMENT TO THE SCENE

For pertinent reasons, an auto-iris lens was ideal for the ELL video camera and this project; however, the ELL video camera's auto-iris lens does have some significant limitations. The ELL video camera's auto-iris lens automatically controls the amount of light that comes through the camera's lens to its imaging sensor. The larger the iris opening

(aperture), the more light can pass through to hit the image sensor and vice versa. Due to the nature of the underwater experiments in this study, an auto-iris lens was fitting, considering that the illumination throughout the water column changed drastically with depth, which allowed the ELL video camera to adjust automatically and optimize its images to these changes. One of the limitations of the ELL video camera's auto-iris lens is that the user has no control over it. Another limitation occurs when the illumination changes unpredictably from high to low illumination or vice versa, either before a vertical cast, as the ELL video camera descends or ascends through the water column, or in areas of high bioluminescence concentration. Continuous changes in illumination cause the ELL video camera's auto-iris to constantly adjust, producing unrepeatable image exposure when testing the camera's image quality. For example, the ELL video camera's lens aperture will adjust differently each time it records the same scene in the same medium with the same lighting, generating different MTF results consistently. Lastly, it is indeterminate how long the ELL video camera takes to adjust in a dynamic ocean environment, further complicating image quality analysis tests.

C. MTF CAMERA MODEL—THREE SCENARIOS

The results of the vertical casts performed in Monterey Harbor and Monterey Bay demonstrated three scenarios of how artificial light, without bioluminescence influence, and with bioluminescence influence, affects the MTF as a function of water depth under natural illumination at night (Figure 18). The red, blue, and green lines for the three scenarios are the linear fit defined by

$$f(x) = p_1 x + p_2 + \varepsilon, \tag{8}$$

where p_1 represents the slope, p_2 represents the y-intercept, and ε is the error associated with the linear regression model. The parameter estimates are shown in Table 1. The capability of the ELL video camera to capture details of the chart at depths up to 37 m is impressive. Moreover, calculating the best linear fit to the casts with bioluminescence indicates that the ELL video camera could capture details of the chart at depths up to approximately 57 m, while without the influence of bioluminescence, the maximum

detection threshold is assumed to be 39 m. The MTF calculation for the Monterey Harbor is incomplete as deeper depths are needed to see the MTF decay; hence there is no variation in the harbor depths, so the extrapolation is not accurate. Nevertheless, the linear fit model for the camera in a nighttime ocean environment is ready for operational use and can be used by the U.S. Navy to predict the camera's performance.

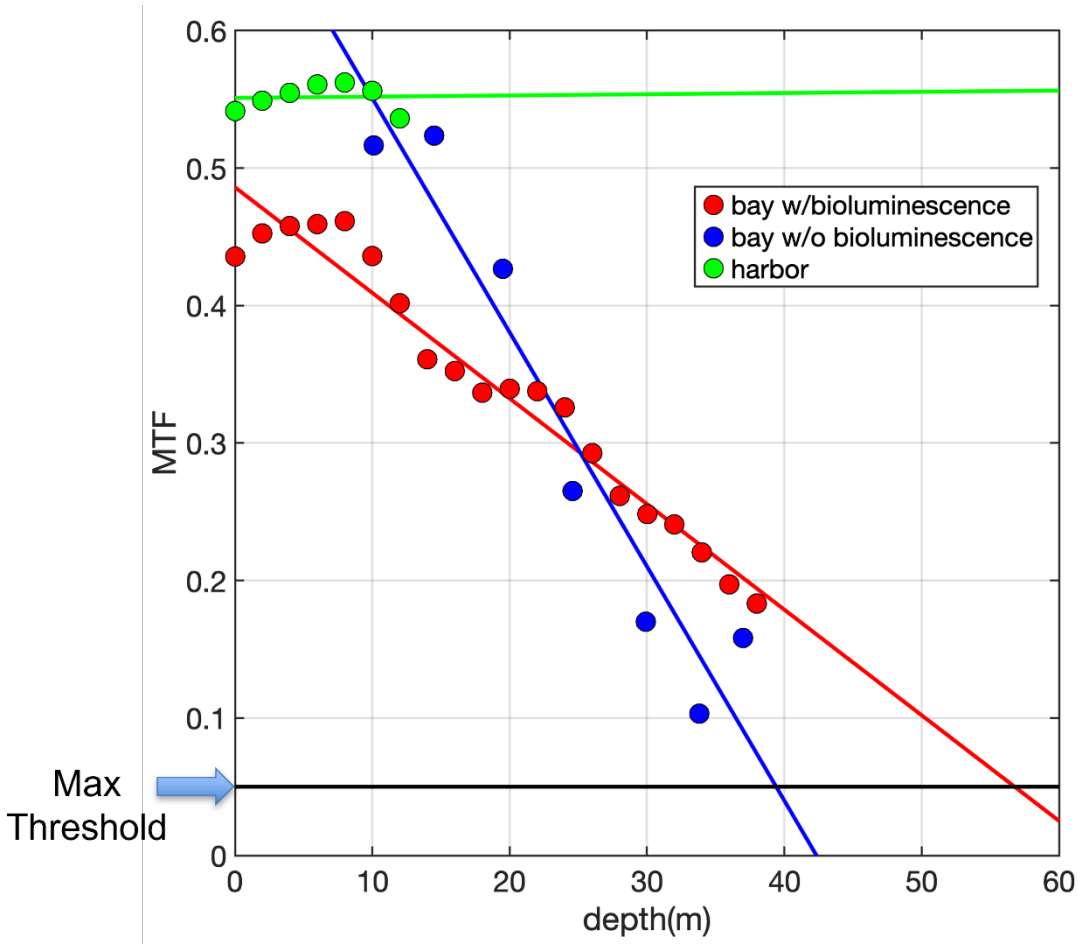

This plot shows three scenarios. Casts in the Monterey Bay with bioluminescence (red circles), without bioluminescence (blue circles), and the Monterey Harbor (green circles). The red, blue, and green lines are the linear fit. The black horizontal line at the bottom of the graph is the maximum MTF threshold, 0.05, where we believe we can no longer see the square wave chart.

Figure 18. MTF camera model—three scenarios.

Table 1. Linear model parameter estimates from the three MTF camera scenarios.

Model Variation (f(x))	Parameter Estimates	
	p_1 (95% Confidence Interval) [MTF/m]	p_2 (95% Confidence Interval) [MTF]
Bay w/ bioluminescence	-0.007682 (-0.008511, -0.006854)	0.4861 (0.4677, 0.5045)
Bay w/o bioluminescence	-0.017030 (-0.022640, -0.011420)	0.7212 (0.5757, 0.8666)
Harbor	0.00008 (-0.002526, 0.002704)	0.5511 (0.5322, 0.5699)

V. CONCLUSIONS AND RECOMMENDATIONS

A. SUMMARY

The great-power competition has exponentially accelerated the development and regulation of new technologies, especially military technologies that further the gap among adversaries and protect the interests of the United States. If the U.S. Navy were to exploit the newfound technology presented in this study, the technology would contribute substantially to the U.S. maintaining its advantage in developing and deploying innovative military capabilities.

This paper discussed techniques and measurement results to evaluate the image quality of the Teledyne Bowtech Limited Explorer Pro Low Light Monochrome Camera's performance in the field as a function of water depth at night in the coastal ocean. In particular, the MTF for the captured images of an in-house developed square wave test pattern was applied to quantify the ELL video camera's performance. Several trials were conducted to carefully select the ideal image quality test pattern that suited the ELL video camera's capabilities. A camera calibration procedure was performed to mitigate the ELL video camera's lens distortion and improve its MTF calculation accuracy. Finally, this project investigated scientific questions through lab and field experiments conducted in the Monterey Harbor and Monterey Bay.

The results of the experiments yielded three significant findings. First, with near-zero lux at the surface, the ELL video camera distinguished the contrast of the square wave test pattern at a maximum depth of 37 m, which resulted in an average MTF of 15% across all spatial frequencies. This result indicated that at a depth of 37 m, 15% of the target information would be transferred to the image information of the ELL video camera. Second, having the camera rest on the ocean bottom significantly reduced the influence/contamination of bioluminescence on the image quality/MTF calculation. All bottom MTFs resulted in a higher MTF when the depth was less than 24.5 m. When the depth was $\geq$ 24.5 m, it did not matter if the ELL video camera was stationary as the lux and target contrast were too low for operational use. Conversely, the bioluminescence increased

the lux and target contrast at depths ≥ 24.5 m, producing higher MTFs than when the ELL video camera was stationary at similar depths. Thirdly, applying the linear regression model to the ELL camera, predicted the maximum depth the camera could operate in a bioluminescence-influenced and non-bioluminescence-influenced ocean environment. The linear regression model for the ELL camera provided valuable information that revealed further research is needed to validate the maximum depth and distance the camera can transfer target contrast in a bioluminescence-influenced and non-bioluminescence-influenced ocean environment under natural night illumination conditions.

B. RECOMMENDATIONS

Most of the camera image quality tests, using test pattern charts, consist of initially capturing images of the test pattern at a set distance and then increasing the distance between the camera and chart until the camera cannot resolve the details on the chart. Furthermore, tests are usually performed with high-resolution cameras in a controlled lighting environment on land. Logistically, this is easier. In comparison, this study maintained a fixed distance between the test pattern and the camera. The measurements quantified the camera's image quality as a function of ocean depth instead of as a function of horizontal distance. In setting the fixed distance, all line pairs on the in-house square wave test chart are overly well-resolved. The ELL video camera could identify all spatial frequencies up to 37 m water depth without frequency decay. Incorporating a square wave test pattern with finer resolution or placing the target pattern farther away would provide better MTF estimates for the ELL video camera. The distance between the target and the ELL video camera was 14.5 cm. Testing the chart at various horizontal distances would resolve the distance that the ELL video camera could detect fine details in the ocean as a function of depth.

An additional recommendation is related to camera quality. Industry-standard COTS cameras have high-definition (HD) image sensors of 1920 (H) x 1080 (V), while the ELL video camera has a standard definition image sensor of 768 (H) x 494 (V). Teledyne Marine, the ELL video camera manufacturer, can leverage its technology's full range (Teledyne Marine 2022) to HD or at least with HD digital outputs and inputs instead

of analog. Though a higher resolution is recommended, it is recognized that the graininess of low-light images might exceed the HD resolution, hence why this has not been developed.

THIS PAGE INTENTIONALLY LEFT BLANK

LIST OF REFERENCES

Allen, E., and S. Triantaphillidou, eds., 2011: *The Manual of Photography*. 10th ed. Elsevier/Focal Press, 566 pp.

Boreman, G. D., 2001: *Modulation Transfer Function in Optical & Electro-optical Systems*. SPIE Press, 110 pp.

Chen, Y., X. Chen, and W. Shen, 2008: A method for measuring modulation transfer function of CCD device in emote camera with grating pattern. Vol. 6829 of *Advanced Materials and Devices for Sensing and Imaging III,* SPIE, 209–215, https://doi.org/10.1117/12.754829.

Coltman, J. W., 1954: The specification of imaging properties by response to a sine wave input. *J. Opt. Soc. Am.,* **44,** 468, https://doi.org/10.1364/JOSA.44.000468.

Dowdy, S. M., S. Wearden, and D. M. Chilko, 2004: *Statistics for Research*. 3rd ed. Wiley-Interscience, 627 pp.

Dugonik, B., A. Dugonik, M. Marovt, and M. Golob, 2020: Image quality assessment of digital image capturing devices for melanoma detection. *Appl. Sci.*, **10**, 2876, http://dx.doi.org.libproxy.nps.edu/10.3390/app10082876.

Fischer, T. A., and J. Holm, 1994: Electronic still picture camera spatial frequency response measurement. *IS&T's 47th Annual Conference/ICPS*, 626–630, https://www.imaging.org/site/PDFS/Standards/ResolutionTools/47th_Annual_pp%20626-630_Fischer.pdf.

Fiske, T. G., and L. D. Silverstein, 2006: Display modulation by Fourier transform: A preferred method. *J. of the Soc. for Information Display*, **14**, 101–105, https://doi.org/10.1889/1.2166827.

Hou, W., 2013: *Ocean Sensing and Monitoring: Optics and Other Methods*. SPIE Press, 251 pp.

Imatest, 2022: Using eSFR ISO Part 1 | Imatest. Accessed 13 February 2022, https://www.imatest.com/docs/esfriso_instructions/#MW.

Leung, C., and T. D. Donnelly, 2017: Measuring the spatial resolution of an optical system in an undergraduate optics laboratory. *Amer. J. of Physics*, **85**, 429–438, https://doi.org/10.1119/1.4979539.

Lin, S.-Y., and W.-H. Chan, 1997: MTF and CTF measuring system for digital still cameras. Vol. 3019 of, *Solid State Sensor Arrays: Development and Applications,* SPIE, 50–57, https://doi.org/10.1117/12.275191.

Liu, J., Z. Yang, H. Huo, and T. Fang, 2018: Camera calibration method with checkerboard pattern under complicated illumination. *JEI*, **27**, 043038, https://doi.org/10.1117/1.JEI.27.4.043038.

Masaoka, K., T. Yamashita, Y. Nishida, and M. Sugawara, 2014: Modified slanted-edge method and multidirectional modulation transfer function estimation. *Opt. Express, OE*, **22**, 6040–6046, https://doi.org/10.1364/OE.22.006040.

MathWorks, 2022: Calibration patterns—MATLAB & Simulink. Accessed 31 March 2022, https://www.mathworks.com/help/vision/ug/calibration-patterns.html.

Miller, J., and A. Al Badi, 2020: Whitepapers—VSI Labs—AV & ADAS Research. Accessed 28 March 2022, https://www.vsi-labs.com/resources/whitepapers.

Mobley, C. D. , 2022: *The Oceanic Optics Book*. Dartmouth, NS, Canada, International Ocean Colour Coordinating Group (IOCCG), 924 pp. DOI: http://dx.doi.org/10.25607/OBP-1710.

Moeller, M. L., 2021: Low-light Camera field evaluation for underwater nighttime operations. M.S. thesis, Dept. of Oceanography, Naval Postgraduate School. 74 pp.

Nill, N. B., 2001: Conversion between sine wave and square wave spatial frequency response of an imaging system. MITRE Center for Integrated Intelligence Systems Bedford, Massachusetts, 44 pp, https://apps.dtic.mil/sti/pdfs/ADA460454.pdf.

Nowinszky, L., and J. Puskás, 2012: Light-trap catch of the harmful moths depending of moonlight in North Carolina and Nebraska states of USA. *ISRN zoology*, **2012**, 1–6, https://doi.org/10.5402/2012/238591.

Parush, A., M. S. Gauthier, L. Arseneau, and D. Tang, 2011: The human factors of night vision goggles: Perceptual, cognitive, and physical factors. *Rev. of Human Factors and Ergonomics*, **7**, 238–279, https://doi.org/10.1177/1557234X11410392.

Roland, J. K. M., 2015: A study of slanted-edge MTF stability and repeatability. *IS&T/SPIE Electronic Imaging*, San Francisco, California, USA, 93960L, https://doi.org/10.1117/12.2077755.

Task, H. L., 2001: Night vision goggle visual acuity assessment: results of an interagency test. Vol. 4361 of, *Helmet- and Head-Mounted Displays VI,* SPIE, 130–137, https://doi.org/10.1117/12.437987.

Task, H. L., and A. R. Pinkus, 2007: Theoretical and applied aspects of night vision goggle resolution and visual acuity assessment. Vol. 6557 of, *Head- and Helmet-Mounted Displays XII: Design and Applications*, SPIE, 183–193, https://doi.org/10.1117/12.721365.

Teledyne Bowtech Ltd, 2020: Teledyne Bowtech explorer pro low light monochrome camera, 4 pp. Accessed 20 March 2022, http://www.teledynemarine.com/explorer-pro.

Teledyne Marine, 2022: About us. Accessed 25 April 2022, http://www.teledynemarine.com/about-us.

Wang, F., F. Cao, T. Bai, N. Cao, C. Liu, and G. Deng, 2014: Experimental measurement of modulation transfer function of a retina-like sensor. *OE*, **53**, 113106, https://doi.org/10.1117/1.OE.53.11.113106.

Zhang, X., T. Kashti, D. Kella, T. Frank, D. Shaked, R. Ulichney, M. Fischer, and J. P. Allebach, 2012: Measuring the modulation transfer function of image capture devices: what do the numbers really mean? Vol. 8293 of, *Image Quality and Sys. Perfor. IX, SPIE*, 64–74, https://doi.org/10.1117/12.912989.

THIS PAGE INTENTIONALLY LEFT BLANK

INITIAL DISTRIBUTION LIST

1. Defense Technical Information Center
   Ft. Belvoir, Virginia

2. Dudley Knox Library
   Naval Postgraduate School
   Monterey, California